Palaeogeography, Palaeoclimatology, Palaeoecology 697 (2026) 113915

Contents lists available at ScienceDirect

Palaeogeography, Palaeoclimatology, Palaeoecology

journal homepage: www.elsevier.com/locate/palaeo

A new astronomical time scale for the early Triassic: Timing of biotic recovery in NW Pangaea

Chen Shen [a,*], Shane D. Schoepfer [b], Charles M. Henderson [c], Ranjot S. Brar [c], Qinwan Chong [a], Thomas F. Moslow [c]

[a] CNOOC Research Institute Ltd., Beijing, 100028, China
[b] Geosciences and Natural Resources Dept., Western Carolina University, Cullowhee, NC 28723, USA
[c] Department of Earth, Energy, and Environment, University of Calgary, Calgary, AB T2N 1N4, Canada

ARTICLE INFO

Editor: L Angiolini

Keywords:
End-Permian
Extinction
Lower Triassic
Biotic recovery
Milankovitch cycles
Obliquity
Anoxia

ABSTRACT

This study establishes a new, high-resolution astronomical time scale for the Early Triassic, based on a continuous 395 m core of the Montney Formation in northeastern British Columbia. This novel age model allows more precise dating of episodes of anoxia and biotic recovery following the end-Permian mass extinction on the northwestern margin of subtropical Pangaea. Elemental data derived from x-ray fluorescence spectroscopy at centimeter-scale resolution provide a high-resolution geochemical record that can be calibrated and chronostratigraphically correlated with conodont biostratigraphy and carbon and nitrogen isotopic records from the same core.

This study uses the elemental dataset (>37,000 measurements of 30 elements) to perform spectral analyses, which demonstrate cyclical components throughout the entire succession. Cyclostratigraphic analyses of Ca and Rb/(Rb + K) chemical element series reveal clear sedimentologic cycles, interpreted to represent a 405-kyr long-eccentricity cycle, a 100-kyr short-eccentricity cycle, a 33-kyr obliquity cycle, and a 20-kyr precession cycle. Anchoring these cycles to the onset of the latest Permian transgression at the base of the Montney Formation (252.0 Ma), the ages of the Griesbachian/Dienerian, Dienerian/Smithian (Induan/Olenekian), Smithian/Spathian, and Spathian/Anisian (Olenekian/Anisian) boundaries are estimated at 251.76 ± 0.1 Ma, 250.93 ± 0.1 Ma, 249.06 ± 0.1 Ma and 247.1 ± 0.1 Ma, respectively. This ATS differs from the current international chronostratigraphic chart but closely matches recent revisions to Early Triassic geochronology; it yields an independent estimate for the age of the base Anisian that matches recent estimates from South China within 50 kyr. An increase in pelagic biocalcification during early Smithian (~250.6 ± 0.1 Ma) reflects the development of planktic calcispheres as a significant carbon sink and is sensitive to the obliquity cycle. Modulation of obliquity cycles by other orbital components may have regulated the timing of biotic recovery events in the Slide Mountain Ocean throughout the Early Triassic.

1. Introduction

The end-Permian mass extinction (EPME) was the most severe biodiversity crisis of the Phanerozoic, resulting in significant loss of marine and terrestrial taxa. After the destruction of the EPME, the Induan interval of the Early Triassic represented a new start, in which biodiversity could begin to recover. While environmental stresses generally ameliorated throughout the Early Triassic, biological recovery was prolonged and was interrupted several times by episodes of global warming and oceanic anoxia (Sun et al., 2012; Li et al., 2016a; Schoepfer et al., 2024; Zhu et al., 2025). This interval has great potential to provide meaningful analogues to modern climate and biodiversity changes, but our understanding of the dynamics and rates of recovery are currently constrained by an unclear chronometry.

Studies of the Permian-Triassic transition in South China indicate that the EPME occurred within a < 60 kyr interval of time, beginning 251.941 ± 0.037 million years ago (Burgess et al., 2014; Shen et al., 2019). However, the age framework for the Early Triassic recovery remains less precise, with proposed durations ranging from 0.7 to 2.2 Myr for the Induan Stage and 3.2 to 4.0 Myr for the Olenekian Stage (Burgess

* Corresponding author.
E-mail address: cshen59@126.com (C. Shen).

https://doi.org/10.1016/j.palaeo.2026.113915
Received 24 September 2025; Received in revised form 17 May 2026; Accepted 20 May 2026
Available online 24 May 2026

et al., 2014; Galfetti et al., 2007; Wu et al., 2012; Cohen et al., 2013; Ogg et al., 2020; Leu et al., 2025). This study proposes a novel age model for the Early Triassic based on cyclostratigraphic analysis of a continuous core of the Montney Formation, which will allow more precise and accurate dating of recovery from the EPME in NW Pangea.

Stratigraphic successions can record terrestrial responses to astronomical forcings, including changes in the Earth's orbit and spin vector called Milankovitch cycles (Berger, 1988). These cyclical orbital and obliquity variations affect global climate conditions through changes in seasonality and the distribution of solar radiation around the Earth. Identification of these cycles preserved in the geologic record can yield a high-resolution astronomical time scale and constrain the rates of paleoclimatic and paleoecologic change (Hinnov and Hilgen, 2012). While sedimentary cycles of astronomical origin have been identified in the Early Triassic (Yang and Lehrmann, 2003; Wu et al., 2012; Guo et al., 2008; Li et al., 2016a; Li et al., 2016b; Kozur and Weems, 2011), most studies have relied on single proxies.

This study is a high-resolution cyclostratigraphic analysis of the Lower Triassic Montney Formation using multiple proxies, based on elemental variations measured via x-ray fluorescence spectroscopy (XRF) in a 395-m continuous 7.5 cm (3.0″) full-diameter core from the c-65-F/94-B-8 well in northeastern British Columbia, Western Canada (Fig. 1). An ITRAX core scanner was used to measure 30 elements at over 37,000 horizons, providing over 1.1 million geochemical measurements at centimeter resolution. This extremely high-resolution dataset provides a rich record of paleoenvironmental proxies that has already been used to reconstruct the depositional history at this location (Schoepfer et al., 2024).

The studied core is notably continuous, with no observed missing intervals (Moslow et al., 2018). The lack of intraformational unconformities or disconformities is confirmed by regional wire-line log cross-section correlations for the Montney Formation, which represents the third largest unconventional natural gas deposit globally (Baniak et al., 2023). The Induan-Olenekian (Dienerian-Smithian substage) boundary is transitional and is interpreted as the conformity correlative to a sequence boundary observed in shallower-water sections. (Zonneveld and Moslow, 2018). While the Smithian-Spathian boundary in the c-65-F/94-B-8 core is abrupt, it is non-erosional at c65F, in contrast to sites up-dip toward the east (Moslow et al., 2018; Baniak et al., 2023 see their Fig. 10A). Wireline log correlations indicate that the Griesbachian to lower Dienerian interval is thin and probably condensed. The core is thus an outstanding opportunity to examine a complete sedimentologic and stratigraphic record of the entire Lower Triassic.

This remarkably complete dataset was used to develop an ATS, using the standardized time series of the La2004 ETP model (Laskar et al., 2004) from 245 to 249 Ma to identify potential Milankovitch cycles in the Montney Formation. This floating time scale was then integrated with an existing, detailed chronostratigraphic framework constrained by conodont biostratigraphy and sequence stratigraphic horizons, particularly two well-dated and recognizable anchor points: 1) The latest Permian transgression in sea level (corresponding to the base of the Montney Formation), which provided a temporal anchor for astronomical cycles in the Early Triassic, and 2), the base of the Middle Triassic Sunset Prairie Formation, which represents the end of the Early Triassic recovery interval and can be used to test whether hypothesized Milankovitch cycles yield realistic durations for the full Lower Triassic epoch.

The resulting astronomical time scale was then used to constrain the timing of changes in global sea level, temperature, weathering rates, redox conditions, nutrient cycles, and biotic recovery, and to assess temporal variation in sedimentation rates, leading to a better understanding of the steps in biological recovery as they occurred at a mid-latitude site on the northwestern margin of Pangea (Schoepfer and Henderson, 2022; Schoepfer et al., 2024).

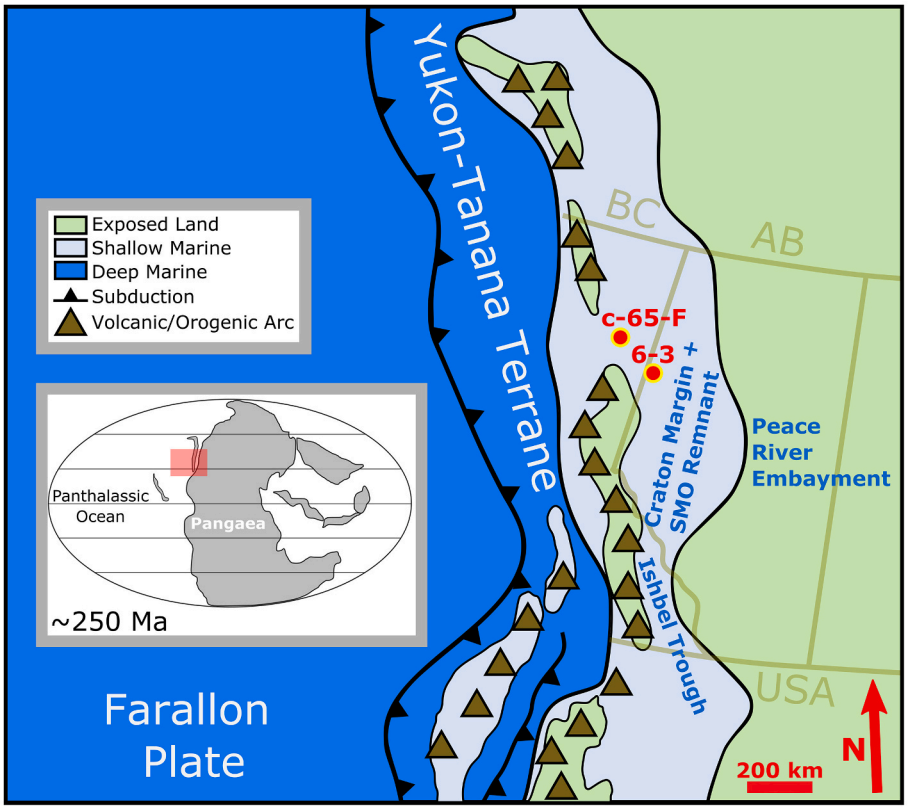

Fig. 1. Schematic palaeogeographic map of western Canada during the Early Triassic (~250 Ma) showing the relative locations of core c-65-F/94-B-8 (56.456250°N, 122.365625°W) and core 6–3-79-13 W6 (55.816190°N and 119.947952°W). Inset at middle left shows the location of the palaeogeographic map on the subtropical western margin of Pangaea. Modified from Schoepfer and Henderson (2022).

2. Geologic background

2.1. Geologic setting

During the Early Triassic, the western margin of the North American Craton formed the northwestern coast of the supercontinent Pangea, fronting on the Panthalassic (i.e., proto-Pacific) Ocean, the world's largest ocean basin at the time (Henderson et al., 2018; Moslow et al., 2018). The Lower Triassic Montney Formation was deposited in the Peace River Embayment (Davies et al., 1997) (Fig. 1), a structural sub-basin within the broader Western Canada Sedimentary Basin (WCSB), from approximately 252 to 247 Ma (Henderson et al., 2018). Montney Formation sedimentary facies are interpreted to reflect predominantly shallow marine (shoreface through offshore) environments (Moslow et al., 2018), with moderate to high subsidence rates associated with the closure of the Slide Mountain Ocean.

The c-65-F/94-B-8 core, from northeast British Columbia, provides a continuous sedimentary record of Early Triassic deposition in a distal shelf setting (Moslow et al., 2018; Schoepfer et al., 2024). The 395 m core comprises 2-m of the Permian Belloy Formation, 371-m of the Lower Triassic Montney Formation, 11.5 m of the Sunset Prairie Formation (i.e. the 'Anisian wedge') and 10.5 m of the overlying Anisian Doig Formation phosphate zone (Moslow et al., 2018).

The Montney Formation, like other Lower Triassic successions worldwide, comprises three 3rd-order depositional sequences (Davies et al., 1997; Moslow et al., 2018; Fig. 2). Beyond sequence stratigraphic surfaces, age control of the Montney and stratigraphic correlations to other sections are determined via conodont biostratigraphy, derived from core samples and in one case, core pseudo-cuttings. Regional biostratigraphic correlations and global chronostratigraphy are summarized below, with additional detail provided in the Supplementary Text.

2.2. Biostratigraphic correlation and chronostratigraphic framework

The c65F core exhibits many marine flooding surfaces with four being particularly distinctive including the basal Montney transgression (uppermost Permian), the top of a widely correlated *Claraia* biostrome (base-Olenekian Stage or Smithian substage), a distinct surface separating middle and upper Montney (base-Spathian substage), and the base of the Sunset Prairie Formation (lowermost Anisian). Many samples did not yield conodonts at c65F but some yielded particularly distinctive conodonts at the base of the Triassic and base-Spathian (Moslow et al., 2018). Another core (6–3; Fig. 1) yielded numerous conodonts with 80% of the 87 samples productive. The many marine flooding surfaces at 6–3 can be correlated with those at c65F, providing a method to interpolate taxon ranges between the two cores (discussed in supplementary text; established in Fig. S4). This allowed the correlation of fifteen conodont biozonal intervals (Fig. 2). that are summarized below and explained in more detail in the Supplementary text.

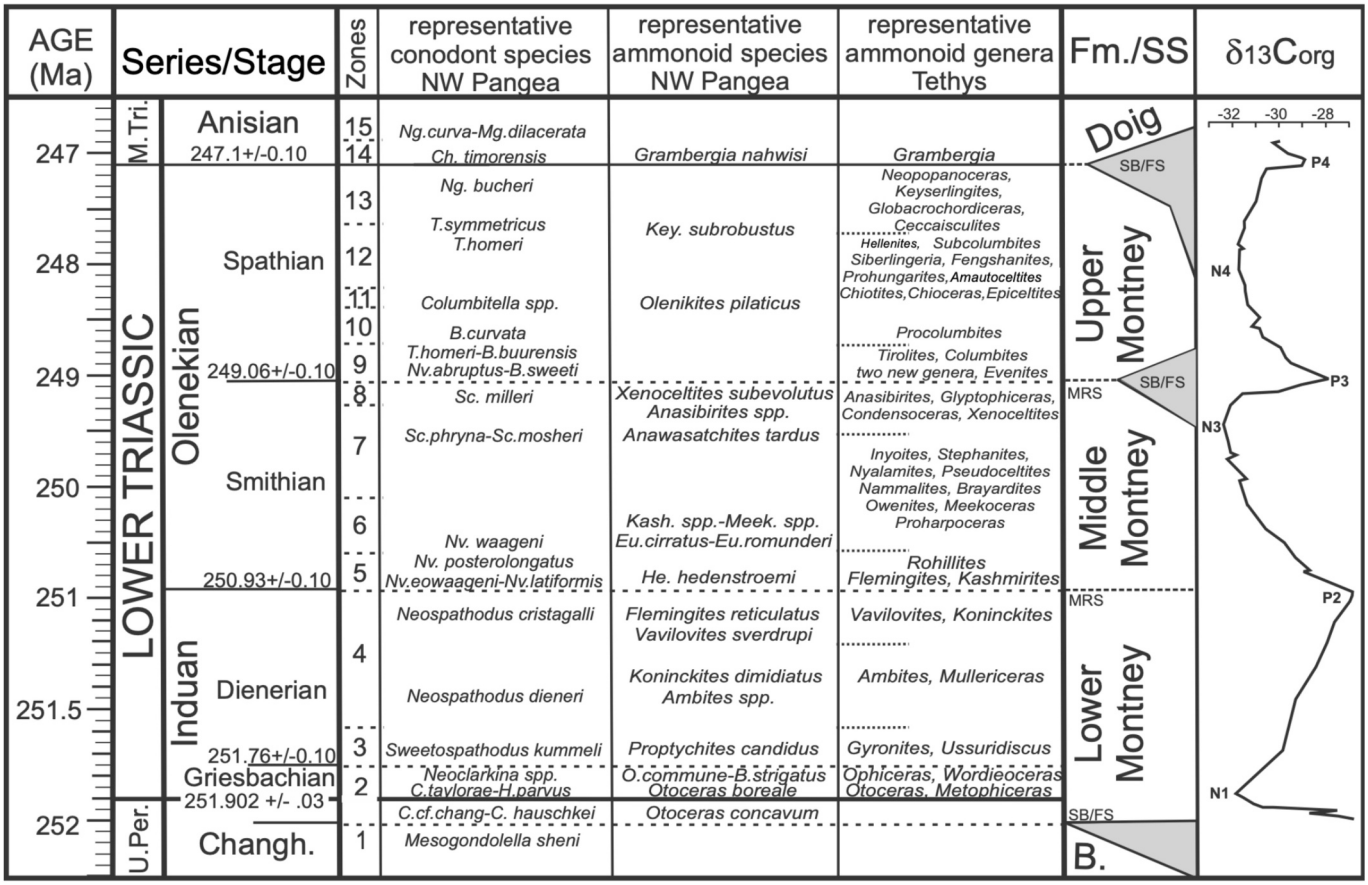

Fig. 2. Lower Triassic stages and time scale (note scale change for 252–251 to provide space for taxon names), conodont biozones developed for correlation in this study (1–15), representative conodont and ammonoid species for NW Pangea, and representative ammonoid genera for the Tethys (modified from Leu et al., 2025), alongside sequence stratigraphy and simplified carbon isotopic curve (from Zhu et al., 2025) for the Montney Formation. Changh. = Changhsingian. Conodonts: *C.* = *Clarkina*, *H.* = *Hindeodus*, *Nv.* = *Novispathodus*, *Sc.* = *Scythogondolella*, *B.* = *Borinella*, *T.* = *Triassospathodus*, *Ch.* = *Chiosella*, *Ng.* = *Neogondolella*, *Mg.* = Magdigondolella. Ammonoids: *O.* = *Ophiceras*, *B.* = *Bukkenites*, *He.* = *Hedenstromia*, *Eu.* = *Euflemingites*, *Kash.* = *Kashmirites*, *Meek.* = *Meekoceras*, *Key.* = *Keyserlingites*. Formations and Sequence Stratigraphy (Fm./SS): B. = Belloy, SB/FS = coplanar sequence boundary and marine flooding surface, MRS = maximum regressive surface (c-65-F core would be positioned on the left side of column and 6–3 core in the middle of the column), grey area indicates missing strata. Carbon isotopic curve notation described later in text but note correspondence of peak positive excursions with stage and substage boundaries.

Chronostratigraphic correlation of the Lower Triassic is largely achieved by the distribution of two fossil groups: ammonoids and conodonts. In many regions ammonoids are the primary biostratigraphic tool (Leu et al., 2025), but in the subsurface of western Canada conodonts have primacy as they are more commonly recovered from core samples given their microscopic size. Some bedding planes in Montney core exhibit ammonoid impressions (see Fig. 6B of Baniak et al., 2023) but these occurrences are rare and the specimens often poorly preserved. Nevertheless, ammonoids and conodonts have been studied in other regions of western and Arctic Canada (Tozer, 1967, 1994; Orchard, 2008) and Fig. 2 provides a summary of these correlations.

Zone interval 1 includes species of *Mesogondolella* including the upper Changhsingian species *M. sheni* in the uppermost Belloy Formation at 6–3 (Henderson et al., 2018). The initial Montney transgression occurs during the latest Permian (Schoepfer et al., 2012; Schoepfer and Henderson, 2022; Henderson et al., 2018), just as it does in most localities around the world. Zone interval 2 is correlated with the Griesbachian substage and includes the co-occurrence of cool-water *Mesogondolella* species and warm-water *Clarkina* species including *C. hauschkei* indicating a major rise in ocean temperature associated with the EPME; a comparable fauna occurs with *Otoceras concavum* in the Sverdrup Basin (Henderson and Baud, 1997). The Permian-Triassic boundary (PTB; base of the Induan Stage) is globally marked by the first occurrence (FO) of the conodont *Hindeodus parvus,* and is correlative with the local first occurrence (FO) of *Clarkina taylorae* in the Lower Montney (Henderson et al., 2018) at c-65-F and 6–3; the latter species occurs with *Otoceras boreale* at Otto Fiord South (Henderson and Baud, 1997). An interval presumably correlating with the upper Griesbachian did not yield conodonts at c65F and 6–3, but elsewhere in the Peace River Embayment species of *Neoclarkina* have been recovered (Henderson et al., 2018). These taxa are associated with the *Bukkenites strigatus* Zone in Arctic Canada (Orchard, 2008), which may extend slightly into the Dienerian substage as the youngest collection in the zone includes the first occurrence of *Sweetospathodus kummeli* at Otto Fiord (Orchard, 2008). Zone interval 3 includes at least four samples with the Dienerian *Sweetospathodus kummeli* in the 6–3 core (Fig. S4). Zone interval 4 includes *Neospathodus dieneri* and *N. cristagalli* and incorporates much of the Dienerian. These taxa are associated with the *Vavilovites sverdrupi* ammonoid zone in the Arctic (Orchard, 2008). Samples from the nearby outcrop belt of NE British Columbia (GSC 56222–56,224) have yielded the ammonoids *Vavilovites sverdrupi*, *Xenodiscoides calnani, and Flemingites reticulatus* (Tozer, 1994) as well as the conodonts (in GSC 56224; pers. comm. Martyn Golding from an internal GSC report) *Neospathodus dieneri* and *N. cristagalli*. The occurrence of

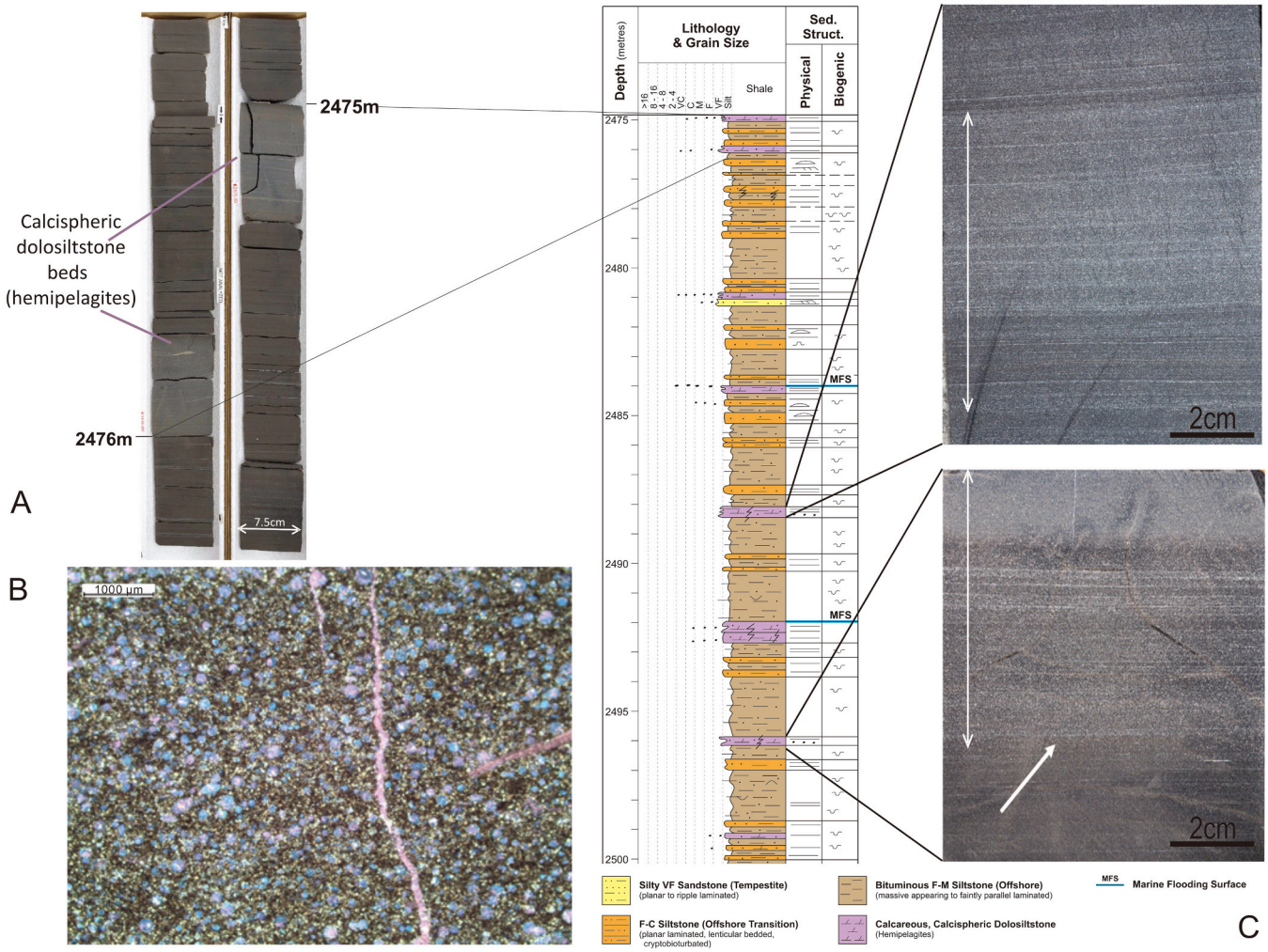

Fig. 3. Panel A. High resolution digital image (right) of a 1.5 m interval of slabbed, full-diameter core from the lower Smithian of the c-65-F/94-B-8 well. Panel B. Potassium ferricyanide-stained thin section of a hemipelagite bed, highlighting an abundance of Fe-calcite calcispheres (blue spherical grains) in a bituminous dolosiltstone matrix. Note small bioclastic fragment and discontinuous vertical calcite-healed fracture (pink stain). Panel C. A 25-m core interval graphic log from the lower Smithian, showing positions of nine ~15 cm-thick calcispheric dolosiltstone beds (hemipelagites, shown in purple), interbedded with dark bituminous siltstone. Close-up core photographs for two of these beds are provided on the right. (For interpretation of the references to colour in this figure legend, the reader is referred to the web version of this article.)

Flemingites in the upper Dienerian is significant. The zone 4/5 boundary coincides with a coplanar maximum regressive surface and marine flooding surface as well as with the P2 carbon isotopic peak (Fig. 3) in our study. This same peak may be slightly higher in the lower Smithian as indicated by Leu et al. (2025).

The Induan-Olenekian boundary (base of informal Smithian substage) is normally correlated using the FO of *Novispathodus waageni* sensu lato. Zone interval 5 is based on biostratigraphy from 6 to 3 that includes first occurrences of *Conservatella conservativus*, *Novispathodus latiformis*, *N. posterolongatus*, and *Nv. eowaageni* (Brar, 2021). This fauna appears to correlate with a pre-*Euflemingites* interval in east-central British Columbia (Orchard and Zonneveld, 2009) and the early Smithian *Rohillites/Flemingites/Kashmirites* interval (Leu et al., 2025). Zone interval 6 includes the extended range of *Nv. waageni* and *Nv. posterolongatus* and correlates with the *Euflemingites romunderi* Zone but with lower diversity compared to the succession in east-central British Columbia (Orchard and Zonneveld, 2009). Younger Smithian units have yielded *Scythogondolella* spp. in the 6–3 core (Brar, 2021) and elsewhere in the Peace River Basin (Golding et al., 2014). Zone interval 7 includes the ranges of *Sc. phryna* and *Sc. mosheri* and Zone 8 includes *Sc. milleri*. These taxa are associated with the *Anawasatchites tardus* ammonoid zone in east-central British Columbia (Orchard and Zonneveld, 2009). Orchard, 2022; his Fig. 4) provides a schematic of the type locality of the *tardus* Zone (Toad River in British Columbia; Tozer, 1994) in which *Sc. milleri* occurs with *Anawasatchites tardus* and with *Xenoceltites subevolutus* 1.5 m higher. A sharp surface another 1.5 m higher yielded very different taxa including *Borinella sweeti*, *B. curvata*, and *Neogondolella* spp. (Orchard, 2022). Golding (2021) also recognized this sharp increase in abundance and diversity at a level described as approximating the Smithian-Spathian boundary at two additional subsurface wells in BC; taxa included *Neogondolella* spp., *Magdigondolella* spp., *Columbitella* spp., *Borinella* spp., *Novispathodus abruptus* as well as *Scythogondolella mosheri* and *Sc. milleri*. The abundance may reflect a transgressive lag or condensation associated with a major Spathian marine flooding surface that may have reworked a few Smithian specimens (*Scythogondolella* spp.). The Smithian-Spathian boundary and zone interval 9 at both c65F and 6–3 cores is correlated by the FOs of *Novispathodus abruptus* and *Borinella* spp. including *B. sweeti and B. curvata*. This level coincides with the P3 carbon isotopic peak (Fig. 3) in our study and approximates the same level in Leu et al. (2023, 2025). Orchard (2022) significantly updated the taxonomy of North American Spathian neogondolellin conodonts. The ranges still require more precision but some of his taxa are recognized in the 6–3 core. Zone interval 10 adds *Triassospathodus homeri*, *Borinella buurensis*, and *Neogondolella* aff. *Bucheri*. *T. symmetricus* and *Columbitella* spp. appear in zone interval 11 in association with a major flooding surface and transgressive surface of erosion. Conodonts are sparse in zone interval 12, which is characterized by the extended ranges of *T. homeri*, *T. symmetricus* and *N.* aff. *Bucheri*. *Neogondolella bucheri* characterizes an uppermost Spathian level in zone interval 13 but may range through much of the Spathian elsewhere (Orchard, 2022). The lower Anisian (zone interval 14) correlates with the occurrence of *Chiosella timorensis* at several localities in the Peace River Embayment (Henderson et al., 2018; Golding, 2021), but not at c65F nor 6–3. The lower Anisian zone interval 15 includes *Neogondolella curva*, *N. hastata*, and *Magnigondolella dilacerata* (Henderson et al., 2018; Golding and Orchard, 2016, 2018).

The Induan-Olenekian boundary and the substage boundaries for Griesbachian, Dienerian, Smithian, and Spathian are not formally defined, but there is an extensive literature considering the correlation of these stratigraphic units. To generate a meaningful time series analysis, it is important to demonstrate how well the 395-m continuous core at c65F can be correlated. In particular, the boundaries of the stages and substages are important to provide a temporal framework. The conodont biostratigraphy has been linked to ammonoid biozones where possible and the resulting framework compares well with many studies. The stage and substage bounding surfaces are well constrained by sequence stratigraphic signatures, conodont biostratigraphy and carbon isotopic excursions and as such provide a template to link the temporal framework determined from time series analysis of the high-resolution dataset from the c65F core.

2.3. The origin of calcispheric dolosiltstones

The Lower Triassic Montney Formation is composed of bituminous, fine to coarse siltstone, as well as very-fine-grained sandstone, calcispheric dolosiltstone, bioclastic siltstone, and phosphorite. All facies were deposited on the proximal through distal portions of a clastic shoreface-to-offshore shelf or mixed clastic/carbonate ramp (Moslow et al., 2018). While siltstone is the predominant lithology throughout the entire Induan and most of the Olenekian interval, these siltstones are interbedded with approximately decimetre-thick calcisphere-rich dolosiltstone beds (Fig. 3) that show well-developed lithologic cyclicity.

Calcispheric dolosiltstone is a carbonate-rich facies common in the Montney Formation, first appearing in the earliest Dienerian and becoming abundant during the early Smithian. The calcispheric dolosiltstone facies is composed of spherical carbonate particles (calcispheres) on the order of 50–200 μm in diameter, densely cemented with calcite or ferroan dolomite.

Davies et al. (2018) suggest that the Montney calcispheres may be the preserved tests of an early form of protodinoflagellate. Concentrations of calcispheres within discrete laminated and inversely graded beds, are interpreted to represent rapid accumulation events, initiated by the proliferation of 'algal' blooms within the photic zone, followed by deposition through hemipelagic suspension settling to the sediment water interface (Fig. 3). The calcispheres are concentrated in laminae and laminae sets, within a matrix of bituminous dolomitic siltstone, mostly of detrital origin (Fig. 3). Calcispheric dolosiltstone beds, comprising many individual laminae, range in thickness from 10 to 30 cm.

Schoepfer et al. (2024) attribute the appearance of calcispheres in the Dienerian to recovering primary productivity. In addition to the Panthalassic Montney Formation, similar-sized calcispheres have been reported across a range of Tethyan settings, including uppermost Griesbachian deposits in Oman (Baud et al., 2012) and lower Dienerian ammonoid-calcisphere wackestones in the Kangshare and Lanchengquxia Formations of southern Tibet (Li et al., 2019a; Shen et al., 2010). Thus, there appears to be a widespread (potentially global) event.

Smaller diameter calcispheres (8–22 μm) are better known from Upper Triassic (upper Carnian and Norian) hemipelagic limestone in Sicily (Preto et al., 2013; Dal Corso et al., 2019), where they are interpreted as calcareous dinocysts. Dal Corso et al. (2019) suggest that Carnian calcispheres may represent a transition to a "Cretan" ocean, in which pelagic biocalcification dominates. The appearance of similar (albeit larger) calcispheres in the Induan, marking an initial recovery of primary productivity, suggests this transition may have started to occur as early as the Griesbachian-Dienerian boundary, and may have served as a major carbon sink during the interval of Early Triassic recovery.

3. Methods

3.1. X-Ray fluorescence spectroscopy

The entire 395-m c-65-F/94-B-8 core was examined with an ITRAX energy-dispersive automated x-ray fluorescence (XRF) core scanner, at Institute National de la Recherche Scientifique, Québec. The measurements were conducted using a molybdenum filament with a voltage of 40 kV and an exposure time of 30 s, generally at centimeter scale. With 30 elements measured at over 37,000 horizons, the dataset includes >1.1 million individual geochemical measurements. The full calibrated dataset is available as Supplementary Table S1 in Schoepfer et al. (2024).

Schoepfer et al. (2024) carefully assessed the quality of various

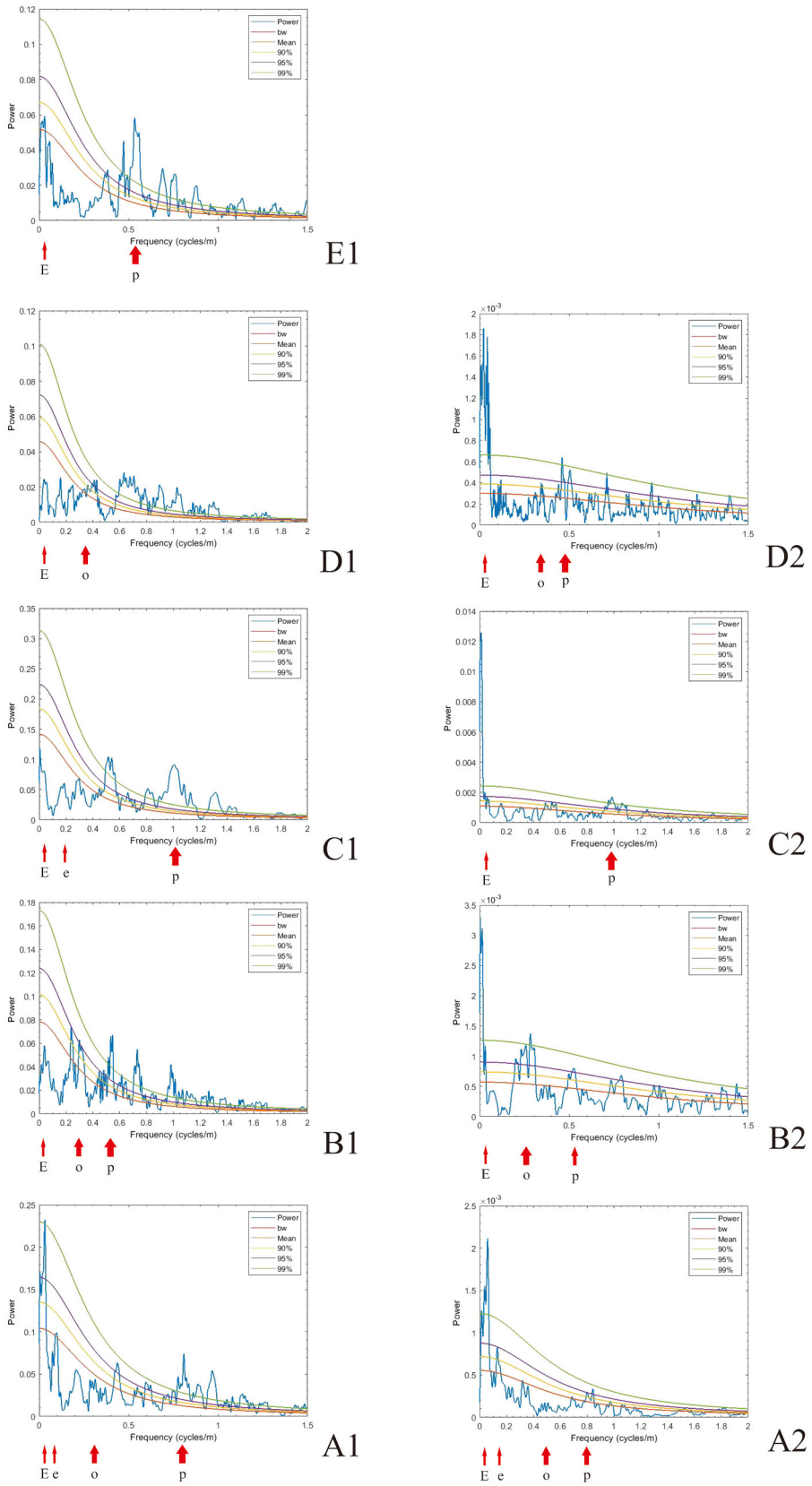

Fig. 4. Results of the 2π MTM power spectral analysis of the untuned XRF data series of the c-65-F/94-B-8 core. Results from the logCa series are shown with A1-E1 (A1: 2576 m to 2495 m; B1: 2495 m to 2415 m; C1: 2415 m to 2365 m; D1: 2365 m to 2285 m; E1: 2285 m to 2181 m.). Results from the Rb/(Rb + K) series are shown with A2-D2 (A2: 2576 m to 2526 m; B2: 2526 m to 2435 m; C2: 2435 m to 2350 m; D2: 2350 m to 2185 m.). (E, e, o and p refer to 405-kyr long eccentricity cycle, ~100-kyr eccentricity cycle, 33-kyr obliquity cycle and 20-kyr precession cycle, respectively.). Spectral peaks were evaluated against robust red noise models at 90%, 95% and 99% confidence levels. (For interpretation of the references to colour in this figure legend, the reader is referred to the web version of this article.)

elemental signals by calibrating X-ray intensities in counts-per-second (cps) to elemental concentrations based on ICP-MS analyses of core-end samples. The strong linear correlation between cps and absolute concentrations for all the elements used in this study ($r^2 = 0.96$ for Ca, 0.87 for K, and 0.73 for Rb; see Table S2 in Schoepfer et al., 2024) indicates that cps values reflect variation in elemental chemistry. Original cps values, rather than calculated concentrations, have been used for subsequent spectral analyses in this study. This does not affect results, as exact elemental concentrations are less important to time series analysis than elemental variation trends.

In the time domain, individual measurements at centimeter intervals theoretically capture a roughly 100-year temporal resolution. The sub-sampled 10-cm dataset used for time series analysis (see Section 3.2 below) captures lithologic variations at an approximately 1000-year resolution. Time-series resolution at century to millennium scale is unprecedented in deep time studies and has the potential to capture the impact of orbital forcing on sedimentary strata at timescales relevant to climate change.

To assess the cyclic drivers of carbonate versus terrigenous deposition, XRF calcium, aluminum, potassium, rubidium and thorium series were initially selected for time-series analysis. The Ca and Rb/K series demonstrated the greatest sensitivity to cyclic variations, and are the focus of this study, while results from thorium and aluminum series are provided in the Supplementary Material.

Calcium is mostly hosted in calcite and dolomite and represents the relative proportion of carbonate in the succession. The carbonate beds are generally autochthonous, with most reflecting the productivity and preservation of calcispheres. Other carbonates, such as a *Claraia* biostrome unit, are also likely to have been closely associated with climatic and oceanographic conditions. Some carbonate beds may be allochthonous, reflecting the frequency and intensity of storms delivering bivalves to offshore settings. However, even these are likely to have been governed by the summer temperature and the distribution of cyclonic belts. Thus, the calcium proxy is an integrated proxy for the effects of climate on carbonate deposition in this succession.

The elemental ratio proxy Rb/(Rb + K) reflects the intensity of chemical weathering, as Rb is more likely to be retained in clays during intense weathering. The intensity of chemical weathering recorded by this proxy varies throughout the c-65-F/94-B-8 core (Schoepfer et al., 2024), which likely reflects changes in atmospheric temperature, precipitation, and/or the pH of meteoric water. All these variables are directly influenced by orbital cycles in climate, with temperature and precipitation/runoff serving as major controls on chemical weathering and erosion.

3.2. Time-series analysis

To identify cyclicity in the Montney succession and detect potential astronomical signals, the following procedures were applied to our XRF elemental data series in “Acycle” (Li et al., 2019b):

(1) XRF datasets were resampled at regular intervals (10 cm) to ensure even sample spacing throughout the dataset.

(2) The base 10 logarithm of the calcium series was taken, to simplify harmonic oscillation features and better detect high frequency cyclicity.

(3) Because estimation and removal of long-term trends is necessary for spectral analysis, the selected XRF series were pre-whitened by removing weighted averages (using “lowess,” “loess,” or “robust loess”).

(4) Trends in the distributions of elements can be used to recognize changes in the sedimentation rate. To identify these trends, XRF series were computed using sliding-window spectral analysis, with an evolutive Fast Fourier Transform (FFT) spectrogram. Based on the distribution of cyclic components, the entire core was divided into intervals. Multitaper method (MTM) frequency analyses were run separately for these intervals.

(5) The power spectra of XRF series were analyzed using MTM frequency analysis, to identify regularly spaced peaks and relate them to the Laskar 2004 solution for predicted orbital eccentricity, obliquity, and precession indices (Laskar et al., 2004).

(6) Spectral peaks were evaluated against robust red noise models at 90%, 95% and 99% confidence levels. These red noise tests are shown with different colors corresponding to different confidence levels in Fig. 4.

(7) Gaussian bandpass filtering was used to support the identification of each potential astronomical parameter and examine its distribution through the entire Early Triassic.

(8) The selected XRF series were tuned to interpreted astronomical cycles with linear interpolation and resampling based on identification of 405-kyr long-eccentricity cycles (Hinnov, 2013).

(9) Power spectra analysis of the tuned records was run to identify significant peaks that align with orbital parameters predicted for the Early Triassic.

(10) An iterative tuning procedure was performed until spectral analysis of optimized stratigraphic models demonstrated convergence, as recognized by stable spectral peaks and coherent orbital-band continuity across the stratigraphic section.

(11) The age of the onset of the latest Permian transgression (252.0 Ma) was selected as an anchor point to build the astronomical timescale for this study (Henderson et al., 2018).

3.3. Stratigraphic anchor points

The new age model for the Early Triassic developed in this study is built around two principal anchor points. The first is the date of the latest Permian transgression, which corresponds to the contact between the Belloy and Montney formations in the c-65-F/94-B-8 core. The date of 252.0 Ma is based on a sequence biostratigraphic correlation with the Penglaitan section in South China, where a latest Permian sequence boundary and marine transgression are clearly recognized in a carbonate interval that includes several ash beds with high-resolution radiometric dates (Shen et al., 2019). The 252.0 Ma age of the transgression is interpolated between radiometric dates of 252.359 Ma and 251.991 Ma (Shen et al., 2019), with the position of the transgressive surface much closer stratigraphically to the younger age.

The latest Permian age of the initial transgression has been shown biostratigraphically in many regions, including Arctic Canada (Algeo et al., 2012) and Western Canada (Schoepfer et al., 2012; Schoepfer and Henderson, 2022). The original Griesbachian succession, as defined in the Canadian Arctic (Tozer, 1967, 1994; Henderson and Baud, 1997), included this latest Permian transgressive succession, indicating that the informal Griesbachian substage boundary does not coincide with the defined base of the Induan Stage. The EPME event also occurs within these transgressive facies and is not related to the hiatus associated with a global regression (Shen et al., 2019).

The second anchor point for our proposed age model is the base of the Anisian Stage (Middle Triassic). This horizon can be readily recognized in core c-65-F/94-B-8, both biostratigraphically (Fig. S4) and lithologically, via the transition to the sandy Sunset Prairie Formation. No assumed age of this boundary is input into our model; instead the ages count upward from the latest Permian transgression, it serves as an independent check on the hypothesized astronomical cycles. If the model is correctly identifying cycles, it should yield a date for the base Anisian consistent with geochronologic ages for this boundary elsewhere in the world. While the base of the Middle Triassic is dated to 246.7 Ma in the 2020 Geologic Time Scale (Ogg et al., 2020), the most recent radiometric dates suggest an age close to 247.1 Ma (Ovtcharova et al., 2015; Leu et al., 2025).

4. Results

4.1. Calcium series cyclostratigraphy

Interbedding of siliciclastic and calcareous (i.e. calcispheric or

bioclastic) siltstones is ubiquitous in the c-65-F/94-B-8 core. This interbedding is reflected in the XRF calcium series, which shows pervasive cyclic rhythms that likely reflect climatic conditions favorable for carbonate production. The XRF calcium series for the lower Griesbachian-lower Smithian interval (2576 m to 2495 m) shows regular cyclicity with wavelengths of ~28.57 m, ~9.80 m, ~3.13 m, and ~ 1.36 m. These fit the expected ratios of Milankovitch-cycle frequencies, and likely represent 405-kyr long eccentricity, ~100-kyr short eccentricity, 33-kyr obliquity, and 20-kyr precession cycles, respectively. From the lower Smithian to upper Smithian (2495 m to 2415 m), the calcium series is characterized by ~36.5 m, ~3.50 m and ~ 1.85 m wavelengths, which are interpreted to be the 405-kyr long eccentricity, 33-kyr obliquity and 20-kyr precession cycles. For the interval spanning the upper Smithian to lower Spathian (2415 m to 2365 m), the power spectrum of the calcium series shows significant peaks at ~18.87 m, ~5.26 m, ~1.55 m, and 0.94–1.02 m, which also may be attributable to the 405-kyr long eccentricity, ~100-kyr short eccentricity, 33-kyr obliquity, and 20-kyr precession cycles. The lower to middle Spathian interval (2365 m to 2285 m), shows ~37.31 m and ~ 3.08 m cyclic components, which likely reflect the 405-kyr long eccentricity and 33-kyr obliquity cycles (Fig. 5). From the middle Spathian to the lower Anisian Stage (2285 m to 2181 m), wavelengths of ~38.5 m and ~ 2.27 m become highly significant, which may represent the increasing importance of 405-kyr long eccentricity and 20-kyr precession cycles

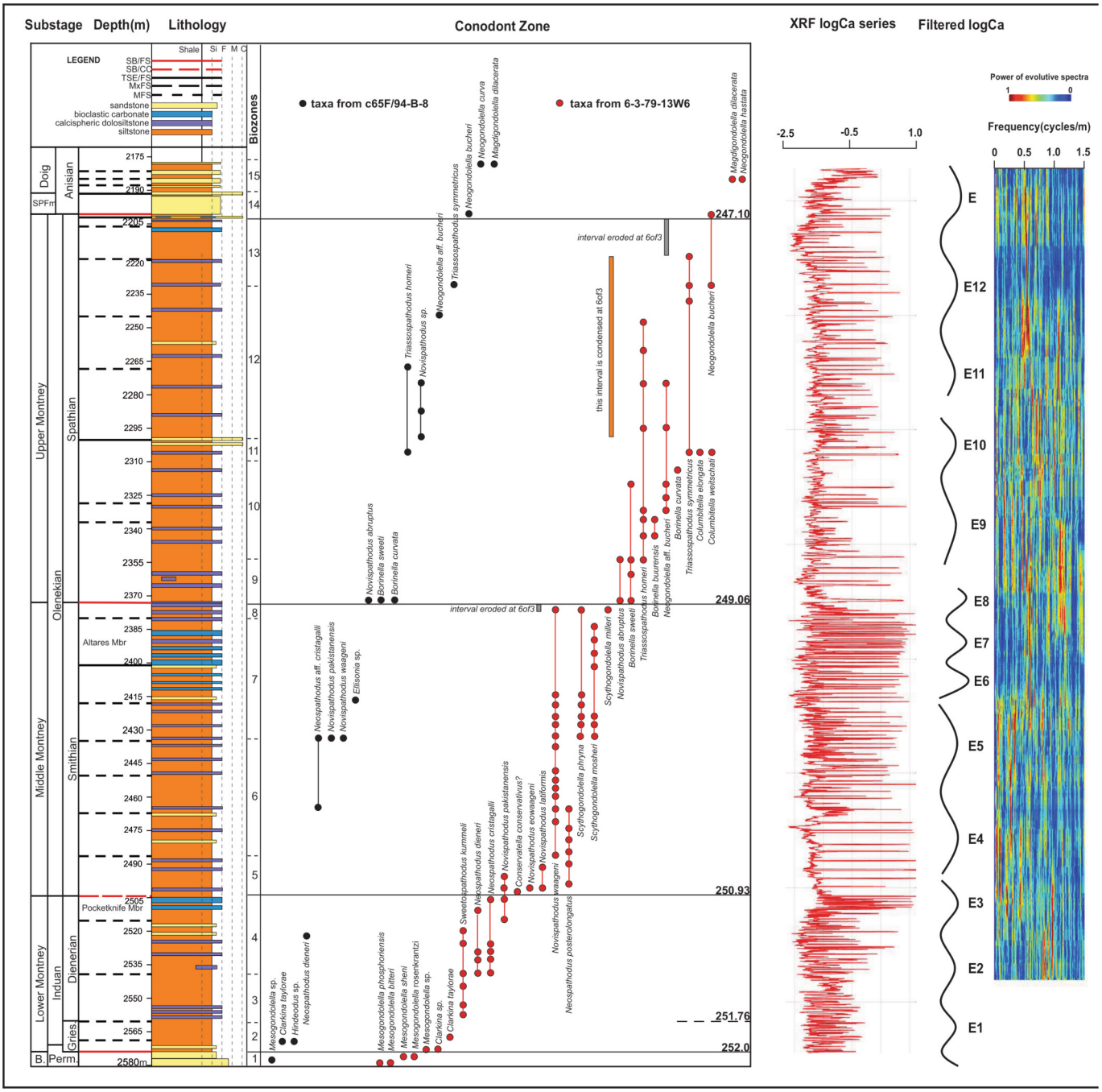

Fig. 5. Lithostratigraphy, conodont biostratigraphy, and interpreted cyclostratigraphy of the Lower Triassic Montney Formation based on XRF log-Ca series, in the depth domain. From left to right: Lithostratigraphy, from Moslow et al., 2018; Biostratigraphy, from Henderson et al., 2018 and Schoepfer et al., 2024; Prewhitened XRF log-Ca series; Filtered cycles are interpreted as 405-kyr long eccentricity (E) cycles (Gaussian filtering). Evolutive FFT spectrum uses 45-m sliding window.

(Fig. 5).

4.2. Rb/(Rb + K) series cyclostratigraphy

Cyclical variations in climatic conditions, including temperature and the intensity of precipitation, may have been driven by orbital forcing, impacting terrestrial chemical weathering. As a result, proxies such as Rb/(Rb + K), which reflect the intensity of chemical weathering, can be used for high-frequency cyclostratigraphic analysis as a potential climate signal. The Rb/(Rb + K) series for the lower Griesbachian-middle Dienerian interval (2576 m to 2526 m) shows regularly cyclic components with wavelengths of ~25.33 m, ~7.69 m, 1.96–2.04 m, and ~ 1.43 m, which are interpreted to represent 405-kyr, ~100-kyr, 33-kyr, and 20-kyr cycles, respectively. From the middle Dienerian to middle Smithian (2526 m to 2435 m), the Rb/(Rb + K) series is characterized by ~32.26 m, 3.57–4.00 m and ~ 1.82 m wavelengths, which are interpreted to be the 405-kyr long eccentricity cycle, 33-kyr obliquity cycle and 20-kyr precession cycles. In the interval from the middle Smithian through the lower Spathian (2435 m through 2350 m), the power spectrum of the Rb/(Rb + K) series shows significant peaks at ~18.58 m and ~ 1.01 m, which can be correlated with the 405-kyr long eccentricity and 20-kyr precession cycles (Fig. 6). The 2350–2185 m

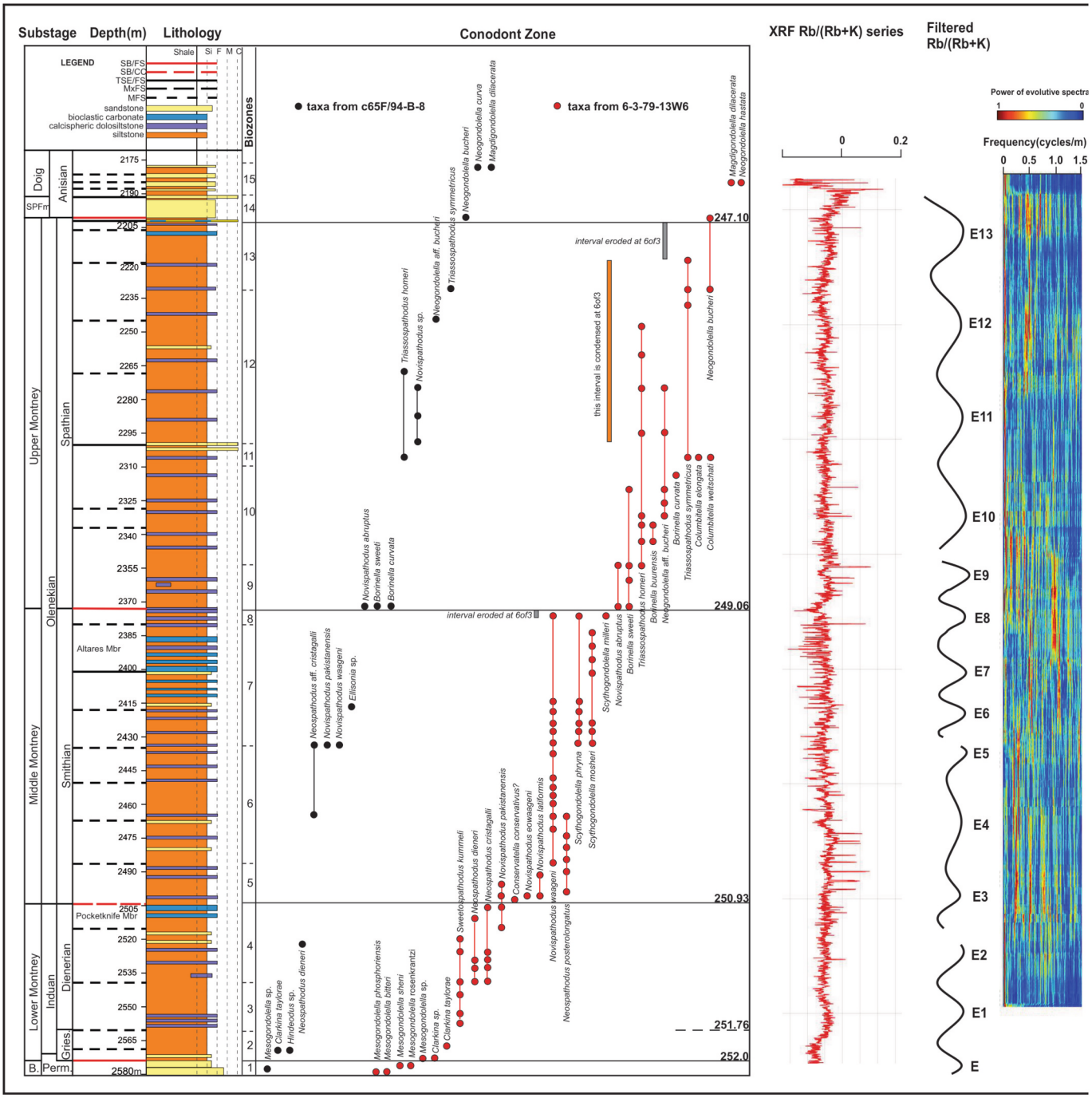

Fig. 6. Lithostratigraphy, conodont biostratigraphy, and interpreted cyclostratigraphy of the Lower Triassic Montney Formation based on XRF Rb/(Rb + K) series, in the depth domain. From left to right: Lithostratigraphy, from Moslow et al., 2018; Biostratigraphy, from Henderson et al., 2018 and Schoepfer et al., 2024; Pre-whitened XRF Rb/(Rb + K) series; Filtered cycles are interpreted as 405-kyr long eccentricity (E) cycles (Gaussian filtering). Evolutive FFT spectrum uses 45-m sliding window.

interval, from lower Spathian to lower Anisian, shows distinct ~40 m, ~2.86 m and, ~2.22 m cyclic components, which are interpreted to represent 405-kyr long eccentricity, 33-kyr obliquity, and 20-kyr cycles (Fig. 6).

5. Discussion

5.1. Milankovitch cycles and astronomical tuning in the time domain

Milankovitch astronomical theory predicts that short-period orbital cycles will be modulated by longer-period cycles (Laskar et al., 2004). The amplitude of the precession and short eccentricity cycles are typically modulated by the 405-kyr long eccentricity cycle, at ~1:20 and ~1:4 ratios of wavelengths respectively. Therefore, the long eccentricity cycle should be detectable in envelope curves derived from amplitude modulation analysis of the 20-kyr precession cycle (Hinnov, 2000; Wu et al., 2012). The 405-kyr long eccentricity cycle is the most stable Milankovitch cycle throughout the Phanerozoic (Hinnov, 2013), and is thus the most readily applicable for establishing and tuning an ATS. In this study, tuning of XRF series to 405-kyr-eccentricity cycles was used to develop a high-resolution astronomical time scale for the substages of the Lower Triassic Epoch.

We assign the ages yielded by this model an uncertainty of ±0.1 Myr (100 kyr). This level of uncertainty integrates three components, namely facies-controlled sedimentation rate changes below the level of resolution captured by the MTM approach described above, error associated with boundary placement (substage definitions) due to the resolution of biostratigraphic sampling, and orbital-response lags capped at 1/4 of a 405-kyr eccentricity wavelength (Hinnov, 2013; Li et al., 2016a).

Two lines of reasoning validate our identification of the 405-kyr long eccentricity cycle. The first is that MTM spectral analysis results of the log-Ca and Rb/(Rb + K) series, when tuned to the 405-kyr long eccentricity cycle, reveal the existence of other cycles with frequencies corresponding to the 4435-kyr, 125-kyr, 95-kyr, 25.3-kyr, 19.7-kyr and 17.0-kyr, astronomical parameters predicted for the Early Triassic in the Laskar 2004 ETP model (Laskar et al., 2004). The second is that the tuning result yields a realistic duration for the full Lower Triassic Epoch, with a date for the base of the Middle Triassic Anisian stage that is within error of the established age of his boundary (see 5.2 below).

5.2. Duration and ATS age of early Triassic stages and informal substages

The biostratigraphically-defined boundaries between Early Triassic substages can be compared to peaks and troughs in the 405-kyr long eccentricity cycles derived from tuning of the XRF log-Ca series (Fig. 7) and Rb/(Rb + K) series (Fig. 8), as well as the Th series (Supplementary Information; Fig. S2). A comparable point in each long eccentricity cycle for all three proxies was plotted against the cored section to produce a time model for the Early Triassic (Fig. 9). The calculated durations can then be anchored to the base of the Montney Formation, which begins with the 252.0 Ma latest Permian transgression (Shen et al., 2019; see time series analysis). The basal 4 m of transgressive Montney facies in core c-65-F/94-B-8 are uppermost Permian in age (252 to 251.9 Ma). These strata include the local extinction of a significant demosponge community, which defines the EPME in northwestern Pangea (Arctic and western Canada; Algeo et al., 2012; Schoepfer et al., 2013), and may have occurred slightly earlier than the Tethyan EPME, which is dated to 251.941 Ma (Algeo et al., 2012; Shen et al., 2019).

The Griesbachian succession, as defined in the type region of the Canadian Arctic, includes both uppermost Permian and lower Induan strata (Henderson and Baud, 1997). This is true in the c-65-F/94-B-8 core as well, where the Griesbachian is ~14 m thick, and is composed of very fine to fine-grained siltstone. The various XRF series considered in this study converge on a duration of 0.24 ± 0.1 Myr for the full Griesbachian succession, or 0.14 ± 0.1 Myr when only the Triassic portion is considered. This age model yields a mean calculated sedimentation rate of 5.8 cm/kyr for this interval, and an age of 251.76 ± 0.1 Ma for the Griesbachian-Dienerian boundary (Fig. 10).

The Dienerian interval is ~55 m thick in core c-65-F/94-B-8, much thicker than the Griesbachian succession. It is mainly composed of laminated siltstone with low carbonate content, with cyclical lithologic rhythms appearing only in the uppermost Dienerian interval. Tuned XRF series indicate that the Dienerian substage has a duration of 0.83 ± 0.1 Myr, yielding a total duration for the Induan stage of 1.0 ± 0.1 Myr (not including the latest Permian part of the Griesbachian). This indicates an age of 250.93 ± 0.1 Ma (Fig. 10) for the Induan-Olenekian boundary (i.e., the Dienerian-Smithian boundary). The mean sedimentation rate for the Dienerian is calculated to be 6.6 cm/kyr, suggesting an increasing sedimentation rate through the Induan (Fig. S3). While sedimentation rates were globally elevated during the Griesbachian, the position of the core in the distal Montney basin results in condensation for this part of the succession. It is interesting that all three XRF proxies provide the same results for the Induan, but they begin to diverge during the early Smithian (Fig. 9).

The Smithian interval is approximately 131 m thick. Lithologic cycles are apparent in the lower Smithian interval, which is composed mainly of bituminous fine to medium siltstone and planar laminated, fine-to-coarse dolomitic siltstone, interbedded with approximately decimetre-thick calcispheric dolosiltstone beds. The calcispheric dolosiltstone beds appear regularly spaced, ~3–4 m apart, following the lowest major occurrence of carbonate in the core, the latest Dienerian *Claraia* biostrome at 2504.5 m (*Claraia* Zone of Moslow et al., 2018). The middle-upper Smithian is dominated by calcareous bioclastic beds (Altares Member; Zonneveld and Moslow, 2018) interpreted as carbonate tempestites as well as calcispheric dolosiltstone beds (Moslow et al., 2018). The succession is interpreted as a mixed carbonate/clastic ramp in a shallow marine (offshore to offshore transition) environment.

The various XRF proxies used in this study show less agreement starting at around 2480 m; this point tunes to an age of 250.6 ± 0.1 Myr and coincides with the sudden increase in pelagic biocalcification by calcispheres. We interpret that the Ca-series signal is increasingly biologically modulated above this horizon, as the calcisphere revolution allows for renewed control of carbonate deposition by primary producers, a significant turning point in biotic recovery following the EPME. This biological modulation alters the Ca time series (blue line; Fig. 9) relative to the series reflecting chemical weathering of detrital material (i.e. Rb/(Rb + K); green line, Fig. 9). As biological productivity is likely to be more sensitive to changes in climate than chemical weathering, and the calcium series yields results consistent with recent geochronology (Fig. 9; see section 5.3 below), we favored the tuned log-Ca series curve for subsequent age determinations.

Tuned XRF series indicate a duration for the Smithian substage of 1.87 ± 0.1 Myr (Fig. 10) with the mean sedimentation rate calculated to be ~7.0 cm/kyr. The anchored ATS projects an age of 249.06 ± 0.1 Ma for the base-Spathian boundary (Fig. 10). The boundary coincides with a coplanar sequence boundary - flooding surface in the Montney Formation (Moslow et al., 2018) with abundant specimens of *Novispathodus abruptus* and *Borinella* spp. immediately above.

The Spathian interval is 171 m-thick (2374 m to 2203 m), making it the thickest substage in core c-65-F/94-B-8, consistent with the significant progradation of the overall Montney succession. The lower Spathian deposits consist of bituminous and dolomitic sandy siltstone to very fine sandstone, phosphorite and calcareous sandy dolostone. Laminated siltstone interbedded with decimetre-thick calcisphere-rich dolostone is also observed in the lower Spathian, like the lower Smithian. The middle to upper Spathian interval includes beds of coarse siltstone to very fine-grained sandstone (Moslow et al., 2018), also reflecting progradation of the Montney succession.

Compiling the results from log-Ca series suggests that the Spathian substage spans 1.96 ± 0.1 Myr (Fig. 10) with a mean sedimentation rate ~ 8.7 cm/kyr (Fig. S3). The accumulation rate varies significantly

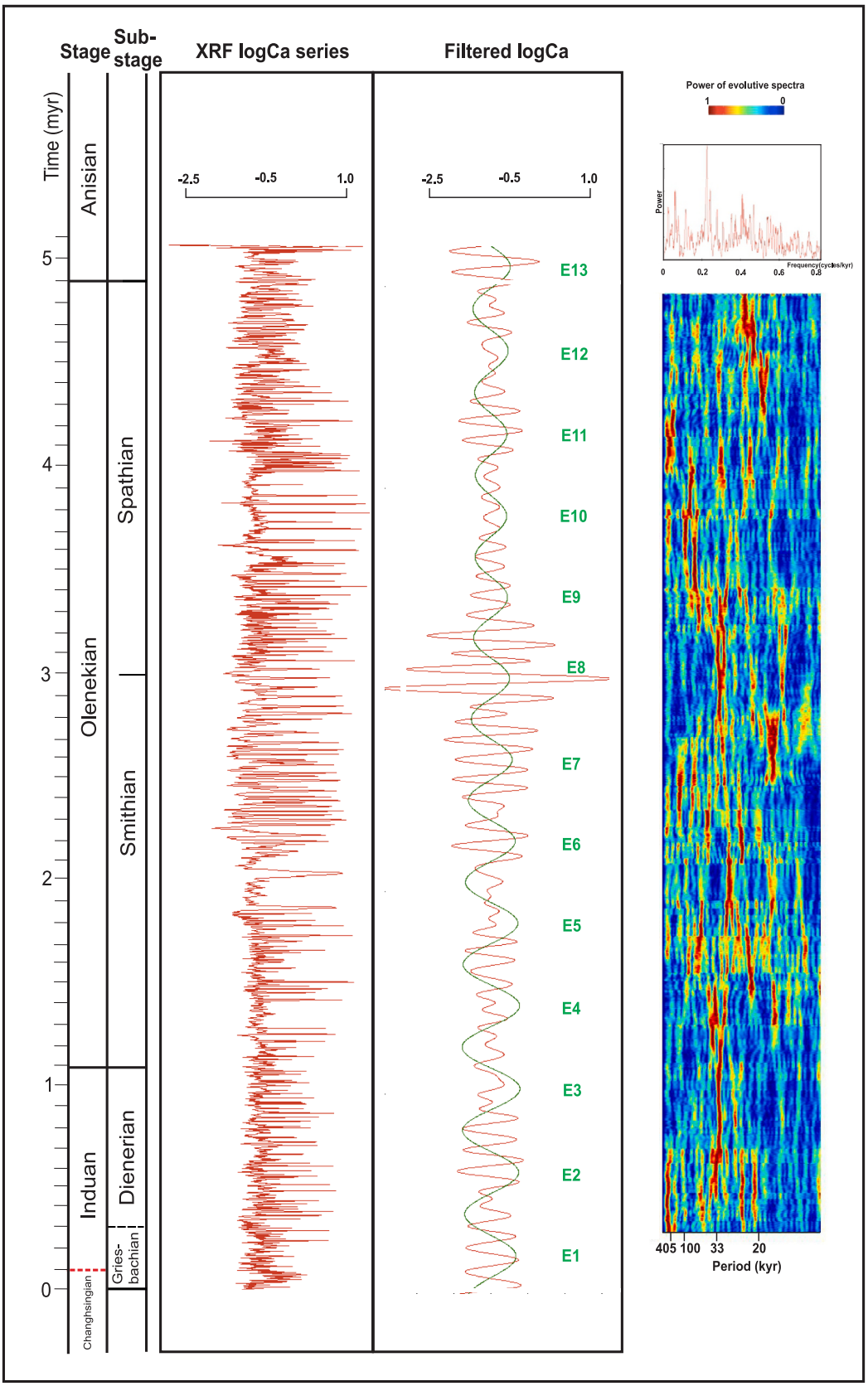

Fig. 7. Cyclostratigraphy of the Lower Triassic Montney Formation based on XRF log-Ca series after tuning to time domain. From left to right: Panel A: Prewhitened XRF log-Ca series after 405-kyr tuning. Panel B: Core c-65-F/94-B-8 tuned XRF log-Ca with filtered 405-kyr (green, E) and 100-kyr (red, e) cycles (Gaussian filter bandpass: 0.0024 ± 0.0002 and 0.01 ± 0.003 cycles/kyr for the E and e cycles respectively).Panel C: Core c-65-F/94-B-8405-kyr tuned XRF log-Ca evolutive FFT spectrum using 500-kyr sliding window. (For interpretation of the references to colour in this figure legend, the reader is referred to the web version of this article.)

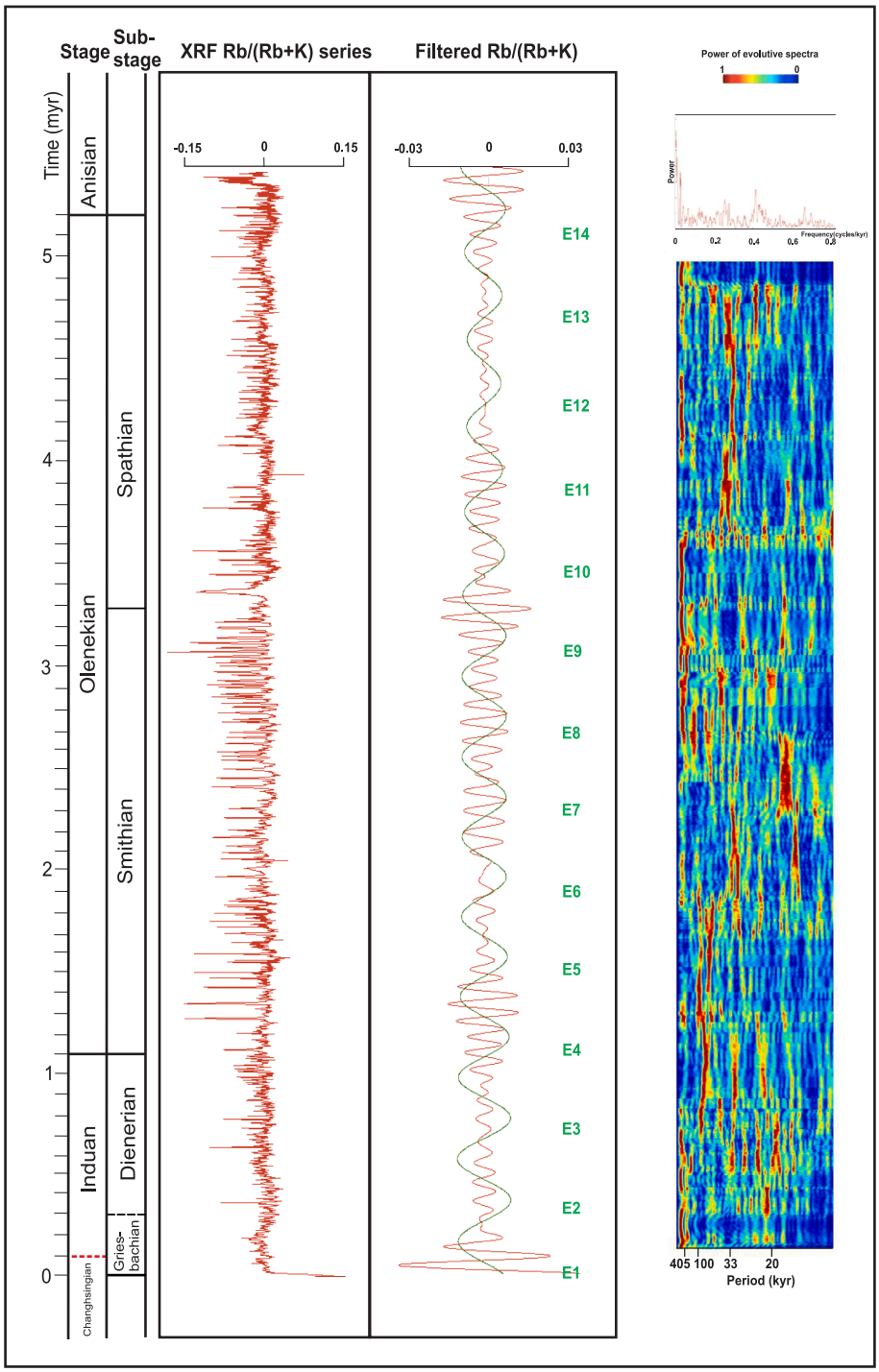

Fig. 8. Cyclostratigraphy of the Lower Triassic Montney Formation based on XRF Rb/(Rb + K) series after tuning to time domain. From left to right: Panel A: Prewhitened XRF Rb/(Rb + K) series after 405-kyr tuning. Panel B: Core c-65-F/94-B-8 tuned XRF Rb/(Rb + K) series with filtered 405-kyr (green, E) and 100-kyr (red, e) cycles (Gaussian filter bandpass: 0.0024 ± 0.0002 and 0.01 ± 0.003 cycles/kyr for the E and e cycles respectively). Panel C: Core c-65-F/94-B-8405-kyr tuned XRF Rb/(Rb + K) series evolutive FFT spectrum using 500-kyr sliding window. (For interpretation of the references to colour in this figure legend, the reader is referred to the web version of this article.)

throughout the Spathian interval, which reflects an unstable and gradually recovering carbonate factory, modulated by changes in accommodation space and regional depositional dynamics (Fig. S3; and see slope of age curve on Fig. 10). The anchored ATS projects an age of 247.1 ± 0.1 Ma for the base Anisian (Olenekian/Anisian boundary), which agrees remarkably well with the 247.05 ± 0.16 Ma age (Fig. 10) reported by Leu et al. (2025).

5.3. Comparing early Triassic age models and geochronologic constraints

The novel Early Triassic ATS developed in this paper indicates durations for the early Induan (i.e. the Triassic part of the Griesbachian), late Induan (Dienerian), early Olenekian (Smithian) and late Olenekian (Spathian) of 0.14 ± 0.1 Myr, 0.83 ± 0.1 Myr, 1.87 ± 0.1 Myr, and 1.96 ± 0.1 Myr respectively. This yields a total duration for the Lower Triassic Epoch of 4.8 ± 0.1 Myr (Fig. 10). Anchoring the ATS to the latest

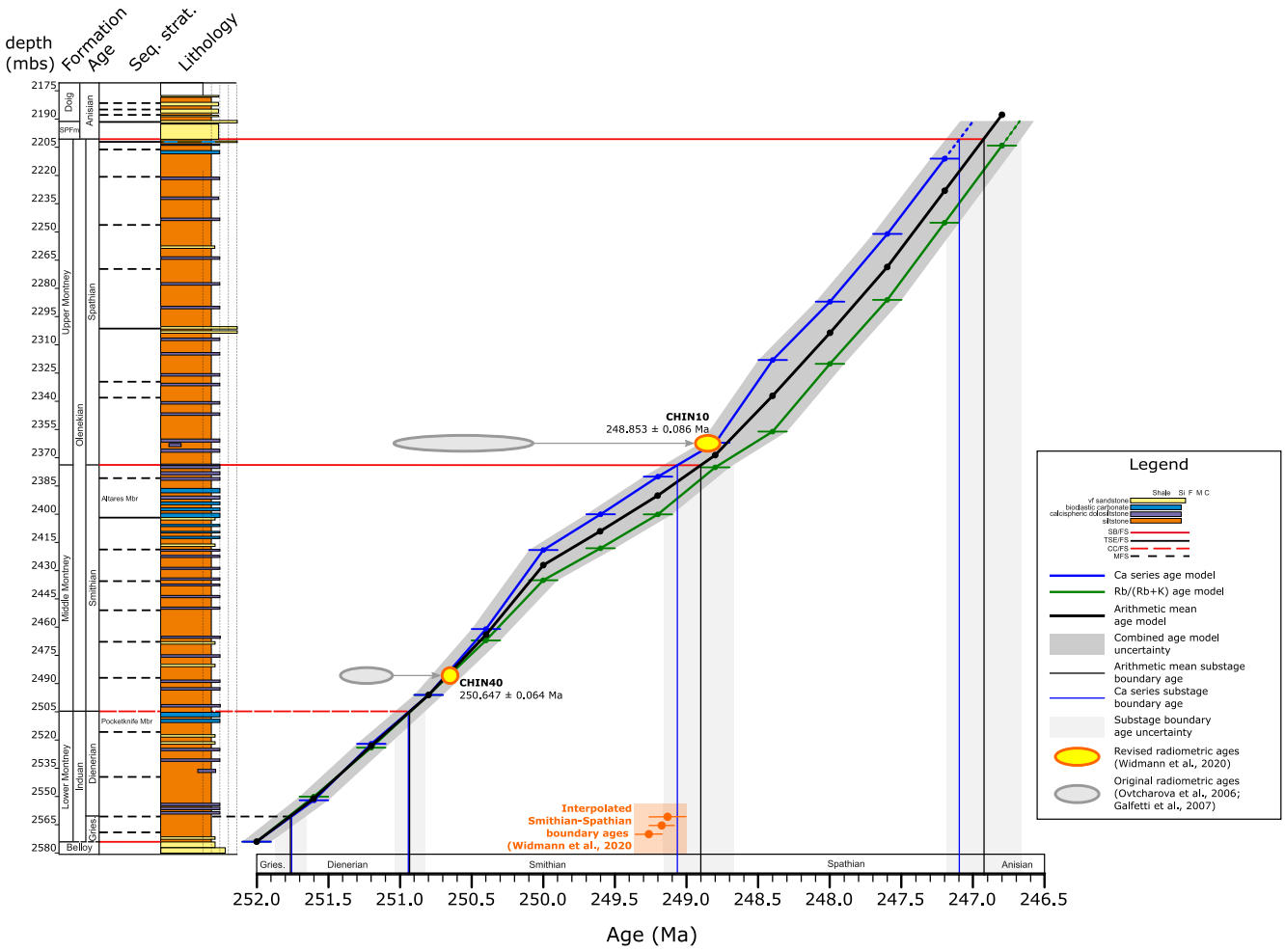

Fig. 9. Integrated age-depth model of the Lower Triassic Montney Formation based on cyclostratigraphic analysis of XRF series, with revised Early Triassic radiometric ages from Widmann et al., 2020 (previous age and uncertainty indicated by grey ellipse and revised ages and uncertainty in yellow). All XRF proxy age models coincide until the early Smithian when they begin to diverge. The geochronologic ages correlate best with the log-Ca series age-depth model. (For interpretation of the references to colour in this figure legend, the reader is referred to the web version of this article.)

Permian transgression (252.0 Ma) provides ages of 251.76 ± 0.1 Ma, 250.93 ± 0.1 Ma, 249.06 ± 0.1 Ma, and 247.1 ± 0.1 Ma for the Griesbachian/Dienerian boundary, Induan/Olenekian (Dienerian/Smithian) boundary, Smithian/Spathian boundary, and Olenekian/Anisian boundary, respectively (Fig. 10).

Our proposed duration for the Early Triassic Induan Stage (1.0 ± 0.1 Myr) is significantly shorter than the ~2.0 Myr Induan shown on the International Chronostratigraphic Chart (v12/2024), which is interpreted from cyclostratigraphic analyses of marine sections at Meishan, Chaohu, Daxiakou, and Guandao in South China (Li et al., 2016a; Ogg et al., 2020), and shorter than the revised astrochronologic duration of 1.57 ± 0.2 Myr from Zhang et al. (2025). However, it is comparable to 1.15 Myr Induan recently proposed by Leu et al. (2025), as well as the 0.9–1.1 Myr Induan of Guo et al. (2008), and the ~1.16 Myr Induan duration of Wu et al. (2012), which were interpreted from cyclostratigraphic analysis of magnetic susceptibility (MS) and anhysteretic remnant magnetization (ARM) records of the Chaohu and Daxiakou sections in South China. It is also comparable with several estimates derived from magnetostratigraphy with ammonite and conodont biostratigraphic constraints (Szurlies, 2007; Lucas, 2010; Hounslow and Muttoni, 2010).

The duration of the Olenekian stage in our tuned ATS is 3.83 ± 0.1 Myr, which is much longer than the 3.2 Myr Olenekian of the International Chronostratigraphic Chart (v2024/12), the 3.1 Myr Olenekian of Li et al. (2016a) and the 3.5 Myr Olenekian of Szurlies (2007), but shorter than the ~4.0 Myr Olenekian of Lucas (2010) and Hounslow and Muttoni (2010). It is nearly identical with the 3.82 Myr Olenekian recently proposed by Leu et al. (2025) for the Nanpanjiang Basin in South China.

The 1.96 ± 0.1 Myr Spathian substage in our model is significantly longer than the ~0.5 Myr Spathian of Wu et al. (2012), based on a cyclostratigraphic study of the Lower Triassic Daye Formation in South China. However it is worth noting that our ATS yields an age for the Smithian-Spathian boundary consistent with recent geochronologic results (Widmann et al., 2020). Two key geochronologic samples (CHIN40 and CHIN10 in Ovtcharova et al., 2006 and Galfetti et al., 2007) have been difficult to reconcile with previous astronomical tuning attempts (Ogg et al., 2020). Zircons from these two samples have been re-dated using current EARTHTIME tracer solution (Condon et al., 2015); the new ages reported in Widmann et al. (2020) and previous ages are plotted on our age model (Fig. 9). The lower Spathian CHIN10 sample has been re-dated to 248.853 ± 0.086 Myr (yellow oval shows uncertainty on Fig. 9; Widmann et al., 2020), consistent only with our calcium-series ATS model.

A modest Induan substage duration (~1.0 Myr) invites reconsideration of Lower Triassic chronostratigraphic subdivision, particularly as the most pronounced biotic reorganization occurs at the Smithian-Spathian boundary (within the Olenekian). Further refinement of the Induan-Olenekian boundary might be warranted given biogeographic complexities in reconciling low-latitude and high-latitude faunal

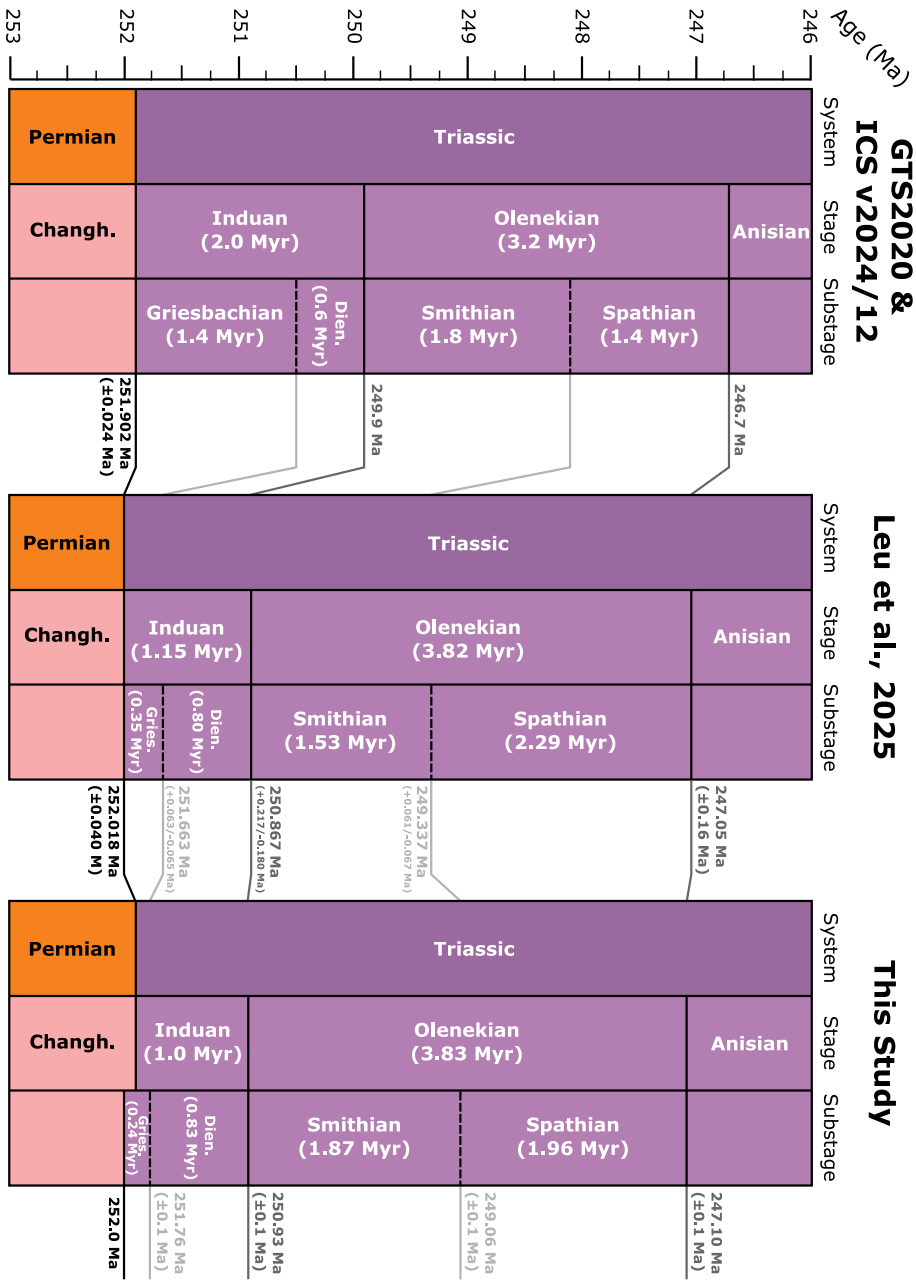

Fig. 10. Early Triassic age models from the International Chronostratigraphic Chart v2024/12 and the Geologic Time Scale 2020 (Ogg et al., 2020), Leu et al., 2025, and this study. Note that in this study, we recognize that the base of the informal Griesbachian substage, corresponding to the latest Permian transgression at 252.0 Ma, is approximately 100 kyr before the PTB.

successions. Despite the variation in the substage durations, the time series analyses presented in this paper yield a total duration for the Early Triassic (4.8 ± 0.1 Myr) consistent with the general consensus, and an age for the Early Triassic-Middle Triassic (i.e., Olenekian-Anisian) boundary (247.1 ± 0.1 Ma) that is in strong agreement with the latest and most advanced geochronologic studies (Ovtcharova et al., 2015 at 247.1 Ma; Arefifard et al., 2025 at 247.2 Ma; Leu et al., 2025 at 247.05 Ma). As the age of this boundary was determined by counting 405-kyr cycles upward from the latest Permian anchor point at 252.0, the precise and realistic age of this boundary is strong and independent support for the accuracy of our ATS.

5.4. *Mechanisms of cyclicity – Evidence from the early Smithian*

The dominance of the obliquity signal during the early Smithian agrees well with the contemporaneous Chaohu and Daxiakou sections in South China (Li et al., 2016b), and suggests obliquity exerted global influence during this interval. The regular ~3–4 m interbedding of siltstone and calcispheric dolosiltstone is interpreted to reflect this obliquity signal (Figs. 3, 11). Cyclicity in the lower Spathian also seems to be related to the obliquity signal.

It has been proposed that greater axial tilt can drive a warmer polar climate by transferring more heat and moisture to high latitudes, at the expense of the tropics (Meyers et al., 2012; Li et al., 2016b). Obliquity forcing can also potentially influence low-latitude wind strength via the meridional temperature gradient, which also affects upwelling (Kuhnt et al., 1997; Meyers et al., 2012). The site of the c-65-F/94-B-8 core represents a relatively low-latitude setting. The palaeolatitude of the Montney depositional basin (Fig. 1) has been estimated at 25–30°N by Davies et al. (1997), and coastal upwelling has been inferred as a

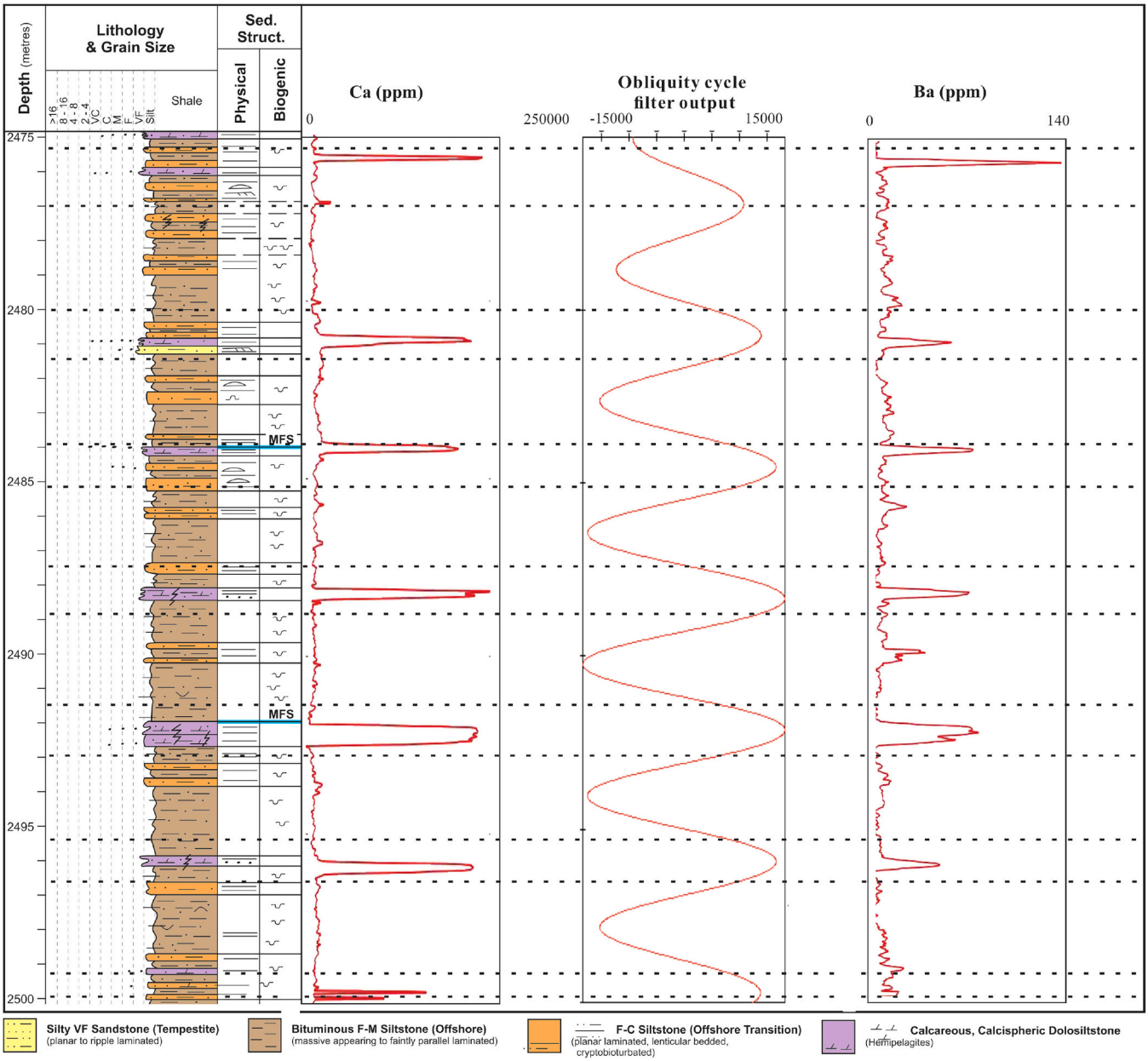

Fig. 11. From left to right: Lithologic column of the lower Smithian interval from 2500 to 2475 m, showing regularly spaced (purple) calcispheric dolosiltstone beds (brown beds are fine to coarse bituminous siltstone; orange beds are sandy coarse siltstone (see Moslow et al., 2018). XRF Ca series (ppm) in the 2500–2475 m interval. 33-kyr obliquity cycle filter output from XRF Ca series in the 2500–2475 m interval. Additional panel shows Ba (ppm) XRF signal ratios for the 2500–2475 m interval. Dashed lines indicate the mutual coupling relationship between calcareous dolosiltstone and obliquity cycle distribution. (For interpretation of the references to colour in this figure legend, the reader is referred to the web version of this article.)

significant factor in the ecology of the basin (Schoepfer et al., 2012).

Calcispheric dolosiltstone intervals correspond to obliquity maxima, while obliquity minima are associated with the deposition of siltstone (Fig. 12). High-tilt intervals would correspond to relatively cooler climate at lower latitudes. Less intense tropical monsoons would likely result in less riverine input to marine environments, providing favorable conditions for the recovery and proliferation of biota. Cooling of surface water at low latitudes would have allowed for more vertical mixing and upwelling of the water column (Fig. 12), providing nutrients to shallow shelf environments (Raymo and Nisancioglu, 2003). During obliquity minima (i.e., less axial tilt), warmer temperatures and increased relative humidity at low latitudes would promote chemical weathering and enhanced detrital influx (Fig. 12). Water-column stratification with suppressed upwelling could limit nutrient mixing and reduce calcisphere productivity (Fig. 12).

Previous studies have observed 1.2 Myr modulation of obliquity throughout the Mesozoic and Cenozoic, and even as early as the Permian (Lourens and Hilgen, 1997; Boulila et al., 2011; Fang et al., 2015). The distribution of filtered 1.2 Myr obliquity modulation cycles detected in the O/T (the ratio of obliquity variance to total variance) of the XRF log-calcium series is comparable with the La2010d astronomical model (Laskar et al., 2011), and the filtered O/T signal from the Chaohu and Daxiakou sections in South China (Li et al., 2016b; Fig. 13).

There is close relationship between 1.2 Myr obliquity modulation maxima and the recurrent "recovery intervals" during the Early Triassic: The early Dienerian shows the initial appearance of calcispheres, the latest Dienerian corresponds with the appearance of *Claraia* biostromes in the Pocketkife member, the peak abundance of calcispheres occurs

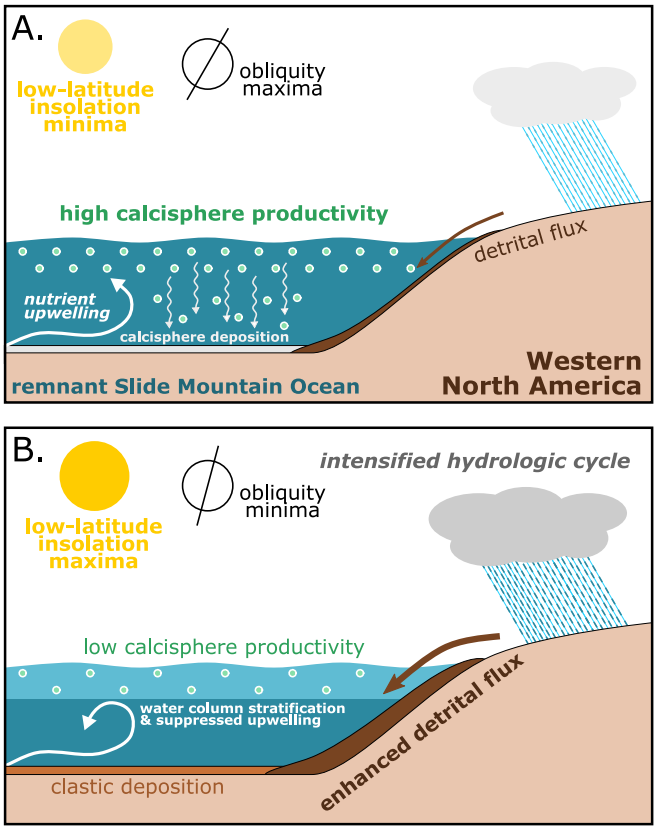

Fig. 12. Schematic model of obliquity forcing of climatic, oceanographic, and environmental conditions for the Montney depositional basin. Panel A represents obliquity maxima, Panel B represents obliquity minima.

during the early Smithian, the late Smithian yields the faunally diverse Altares Member, and the middle Spathian coincides with the amelioration of recurrent anoxia (Schoepfer et al., 2024). This strongly suggests that the timing and pattern of recovery were astronomically paced by long period obliquity modulation (Fig. 13). Additional research integrating biostratigraphy, astronomical tuning, and geochronology may help to resolve issues related to stage correlations and absolute ages of the obliquity modulation peaks in different regions.

5.5. Timing of early Triassic recovery

The EPME and Griesbachian in the c-65-F/94-B-8 core are characterized by dramatic geochemical changes, associated with the termination of coastal upwelling and a decrease in primary productivity (Schoepfer et al., 2024). Nitrogen isotopes, reported here for the first time (Fig. 14), show a rapid decrease across the Permian-Triassic boundary, as is typical from sections across NW Pangea (Schoepfer et al., 2012, Schoepfer and Henderson, 2022) and remain consistently low (<2 ‰) throughout the Early Triassic, only recovering in the Anisian. This is consistent with enhanced nitrogen fixation in response to bioavailable N limitation throughout the 4.8 million years of the Early Triassic. Organic carbon isotopes in the Montney Formation (Zhu et al., 2025; Fig. 14) show a major negative excursion across the Permian-Triassic boundary, but recover rapidly through the Griesbachian-Dienerian interval, reaching a maximum at the Dienerian-Smithian boundary. This series of carbon isotope excursions is broadly consistent with those seen in Lower Triassic strata elsewhere in the world (Arefifard et al., 2025), although the P1 and N2 excursions cannot be distinguished in the condensed Griesbachian interval of c-65-F (Fig. 14).

Euxinic conditions prevailed in the c-65-F/94-B-8 core during the Griesbachian, as they did in many regions of the world (Grasby et al., 2021; Hays et al., 2009; Schoepfer et al., 2024; Song et al., 2014; Zhang et al., 2017). This led to the extinction of the demosponge community prevalent during the latest Permian, and subsequently to a low diversity biota. A delayed biotic recovery characterized many low latitude settings, where microbial-dominated communities (microbialites) developed (Chen et al., 2009; Baud et al., 2021). In contrast, Beatty et al. (2008) described a habitable zone along the northwestern Pangean margin that lacked microbialites, but where wave aeration and frequent storms provided an optimal zone for benthic colonization. This was also true of shallow settings in South China (Song et al., 2011). A significant soft-bodied benthic community existed in the Peace River Embayment during the Griesbachian, preserved as sporadically diverse trace fossils (Zonneveld et al., 2010a, 2010b). The low-diversity nektic community consisted of conodonts, various fishes, and ammonoids.

In the Montney Formation, initial recovery is indicated by the sudden appearance of planktic calcispheres near the base of the Dienerian, 200 kyr after the EPME. However, these calcispheres do not become abundant until the early Smithian, approximately 1.1 Myr after the EPME. This may mark the initiation of a Mesozoic revolution, after which calcareous plankton contributed significantly to carbonate deposition. Indications of macro-biotic recovery include a *Claraia* biostrome unit, which appears in the Pocketknife Member of the Montney Formation, ~1.0 Myr after the EPME (latest Dienerian). A similar lithofacies, with bioclastic packstone to grainstone dominated by bivalves and lingulide brachiopods with rare gastropods (the Anten Coquina), appears in the latest Dienerian and early Smithian of the Montney in more proximal settings (Zonneveld and Moslow, 2018).

Timing this recovery to the latest Dienerian-earliest Smithian is supported by the occurrence of a fossil lagerstatte in the Daye Formation near Guiyang, South China, dated to 250.83 ± 0.07 Ma, ~1.08 Myr after the EPME (Dai et al., 2023). This fauna included a diverse and exceptionally preserved fish and malacostrachan community interpreted as a trophically complex marine ecosystem. A comparable fauna with diverse and fully articulated fishes is preserved in the Peace River Embayment over at least 1000 km of shoreline (Neuman, 2015). The early Smithian conodont *Novispathodus posterolongatus* is reported in both locations (Dai et al., 2023; Orchard and Zonneveld, 2009).

This incipient recovery was partially interrupted by the recurrence of anoxia and euxinia later in the early Smithian (~250.5 Ma; Fig. 9), with a fluctuating redoxcline close to the sea floor (Schoepfer et al., 2024) likely affecting benthic organisms, though deposition of calcispheres continued and indeed reached a peak in this interval. Anoxic events from the earliest Smithian to earliest Spathian are also observed in South China (Song et al., 2012). Evidence for further recovery, during the late Smithian (i.e. ~2.3–2.6 Myr after the EPME), is recognized in the abundant bivalve and brachiopod assemblages of the upper Smithian Altares Member of the Montney Formation (Zonneveld and Moslow, 2018). In contrast, the time interval centered around 249.5 Ma coincides with a "carbonate crisis" at low latitudes elsewhere (Widmann et al., 2020).

Another negative carbon excursion occurs in the Smithian, with the minimum in the latest Smithian followed by a rapid positive excursion approaching the Smithian-Spathian boundary. This $\delta^{13}C_{org}$ minimum may be reflecting the late Smithian thermal event (Zhao et al., 2020; Du et al., 2022), though the strong correlation between $\delta^{13}C_{org}$ maxima and recognized Montney sequence boundaries (Moslow et al., 2018) suggests sea level may be exercising a major control on carbon isotopes in this system. Despite the adverse conditions, calcispheric dolosiltstone continued to be deposited throughout the Smithian.

Fu et al. (2016) determined that the first occurrence of marine reptiles in South China can be dated to 248.8 Ma, using cyclostratigraphy of carbon isotopic values. Although the conclusions of their study were not constrained by conodont biostratigraphy, the interval was interpreted as mid-Spathian. The Montney Formation contains abundant ichthyosaur material in the Altares Member (Zonneveld and Moslow, 2018), which dates to about 249.5–249.3 ± 0.1 Ma and correlates with the late

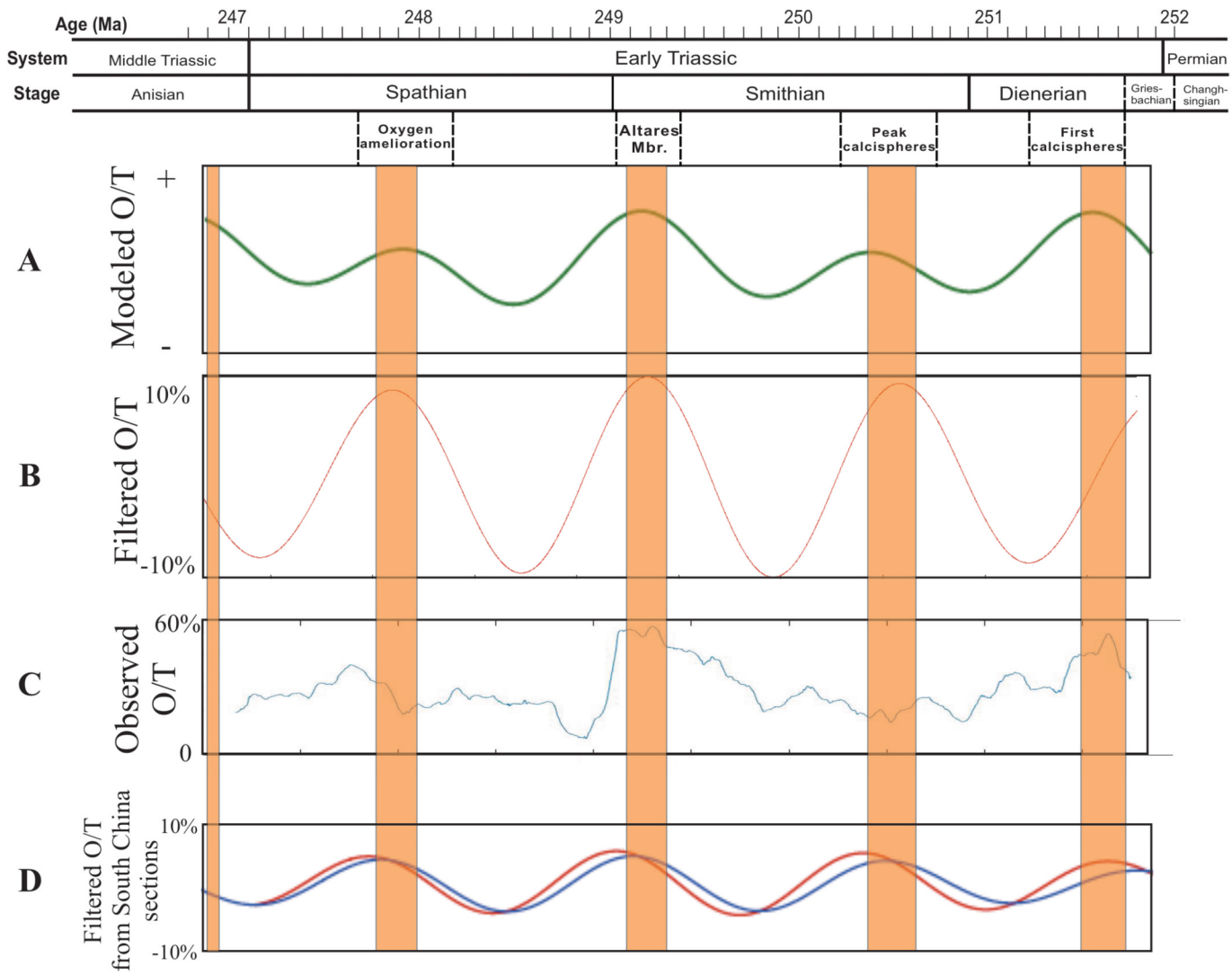

Fig. 13. Early Triassic 1.2 Myr obliquity modulation cycles. Modulation cycles positioned according to geochronometric ages, but corresponding stages and substages differ from Li et al., 2016b. Panel A: Modeled O/T (obliquity power divided by total power) in the La2010d astronomical solution (Laskar et al., 2011). Panel B: Filtered 1.2 Myr obliquity modulation cycles observed in O/T from Montney Formation XRF log-calcium series. Panel C: Calculated O/T series from the XRF calcium dataset. Panel D: Filtered 1.2 Myr O/T cycles from the contemporaneous Chaohu (blue) and Daxiakou (red) sections, South China (Li et al., 2016b). (For interpretation of the references to colour in this figure legend, the reader is referred to the web version of this article.)

Smithian according to the ATS presented in this study and in Leu et al. (2025). This may indicate an earlier appearance of marine reptiles in western Pangea, suggesting that this event was diachronous on a global scale.

Conditions during the Spathian were highly variable, with evidence for upwelling, restriction, and episodic anoxia. The earliest Spathian (basal 15 m) is characterized by high productivity and euxinia. Episodes of anoxia continue into the later Spathian, consistent with records from the same interval in South China (Song et al., 2012), though they notably decrease in intensity from the middle Spathian onward (Schoepfer et al., 2024). The anoxic intervals are punctuated by brief intervals of more hospitable conditions, marked by calcisphere deposition. While the Spathian of the Montney Formation is dominated by local signals related to closure of the Slide Mountain Ocean and the development of the Yukon-Tanana volcanic arc (Schoepfer et al., 2024), this interval is characterized by significant nektic biotic radiation globally, including diversification of conodonts and ammonoids (Song et al., 2018; Zhang et al., 2019).

Increasingly oxic conditions characterize the lower Anisian Sunset Prairie Formation which overlies the Montney (Schoepfer et al., 2024). Significant biotic recovery ~4.8 Myr after the EPME is indicated by diverse trace fossil communities (Furlong et al., 2018) and the occurrences of bivalves, gastropods, lingulide, spiriferid and terebratulid brachiopods, echinoids and crinoids.

6. Conclusions

High-resolution cyclostratigraphic analyses based on multiple XRF series were conducted on a continuous core of the Lower Triassic Montney Formation in the Western Canada Sedimentary Basin. This core is interpreted to represent a complete depositional record of the Lower Triassic along the northwestern margin of Pangea. The cored sedimentary succession reveals clear depositional cycles, observed as calcispheric dolosiltstone beds of hemipelagic origin, which are the product of, and hence a record of, astronomically controlled climate cycles. These lithologic cycles occur throughout the entire Montney Formation, and reflect well-known astronomical forcings, including 405-kyr long-eccentricity, ~100-kyr short-eccentricity, 33-kyr obliquity, and 20-kyr precession cycles. A high-resolution astronomical time scale was established for the entire Lower Triassic Epoch and constrained by

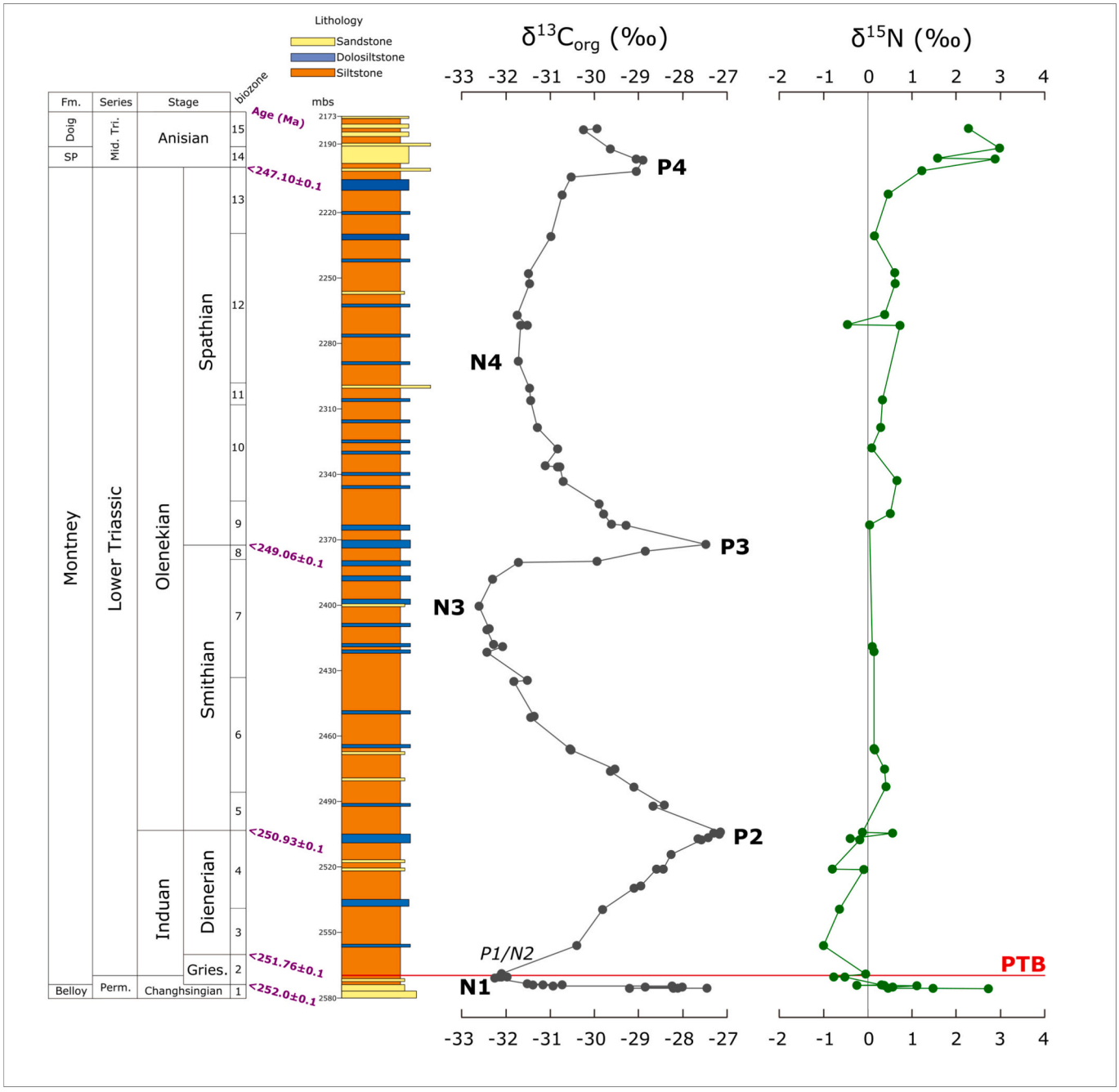

Fig. 14. Organic carbon and nitrogen isotopes from core c65F samples. Organic carbon isotopes are from Zhu et al. (2025). Absolute ages of substage boundaries are from the ATS in this study, biozones are equivalent to those in Figs. 2 and S4. Carbon isotopic excursions numbers (N1, P2 etc.) follow Arefifard et al., 2025 Fig. 1, but our dataset does not resolve P1 and N2 in the Griesbachian (Gries.) and Dienerian. PTB = Permian-Triassic boundary. SP = Sunset Prairie Formation (Fm.)

conodont biostratigraphy and carbon isotopic trends. The resulting ATS suggests that durations for the Griesbachian, Dienerian, Smithian and Spathian substages are 0.24 ± 0.1 Myr, 0.83 ± 0.1 Myr, 1.87 ± 0.1 Myr and 1.96 ± 0.1 Myr, respectively.

When anchored to the base of the Montney Formation, using a 252.0 Ma date for the beginning of the latest Permian transgression, the time scale indicates ages of 251.76 ± 0.1 Ma, 250.93 ± 0.1 Ma, 249.06 ± 0.1 Ma and 247.1 ± 0.1 Ma for the Griesbachian/Dienerian boundary, Induan/Olenekian (Dienerian/Smithian) boundary, Smithian/Spathian boundary, and Olenekian/Anisian boundary, respectively. These ages support, and are supported by, recent independent revisions to the geochronology of this interval. This ATS provides an independent temporal calibration for the timing of Early Triassic recovery events after the EPME in the NW Pangea region.

The EPME in the NW Pangea region is characterized by the extinction of a demosponge community, as most other benthic organisms were already extinct in the region. A significant soft-bodied community preserved as trace fossils sporadically characterized the Peace River Embayment and northwestern margin of Pangea during the earliest Triassic. Initial recovery is suggested by the sudden appearance of planktic calcispheres near the base of the Dienerian, ~200 kyr after the EPME. These calcispheres are sufficiently abundant by the early Smithian (250.6 Ma) to dominate the calcium time series signal, and likely became a major carbon sink affecting climatic amelioration. The appearance of *Claraia* sp. biostromes in the latest Dienerian Pocketknife Member, and resedimented bivalve and brachiopod deposits in the

Altares Member, are dated to 1.1 Myr and 2.5 Myr after the EPME, respectively. A trophically complex, modern-type marine ecosystem including diverse fishes and malacostrachans occurs on both sides of the Panthalassic Ocean about 1.1 Myr after the EPME. The diversification and abundance of marine reptiles (ichthyosaurs) can be dated to between 249.5 and 249.3 ± 0.1 Ma.

The significant dominance of the obliquity signal through the Smithian and lower Spathian interval demonstrates that obliquity forcing was involved in the environmental and biotic upheavals of the Early Triassic and played an important role in sedimentation during that interval. Previous studies (Huybers and Curry, 2006; Li et al., 2018) have suggested that the obliquity signal had an influence on global sea level, climate, and ocean redox conditions during the Early Triassic. As a result, the enhanced obliquity signal seen during the Smithian substage, in the form of regularly spaced (~3–4 m) calcispheric dolosiltstone units, is unique and warrants further investigation to determine the relationship between biodiversity and astronomical signals.

CRediT authorship contribution statement

Chen Shen: Writing – original draft, Visualization, Software, Methodology, Formal analysis, Conceptualization. **Shane D. Schoepfer:** Writing – review & editing, Visualization, Supervision, Methodology, Formal analysis. **Charles M. Henderson:** Writing – review & editing, Visualization, Supervision, Investigation. **Ranjot S. Brar:** Data curation. **Qinwan Chong:** Writing – review & editing, Methodology, Formal analysis. **Thomas F. Moslow:** Writing – review & editing, Resources, Project administration.

Declaration of competing interest

The authors declare that they have no known competing financial interests or personal relationships that could have appeared to influence the work reported in this paper.

Acknowledgements

The project was supported by the University of Calgary, an NSERC Discovery Grant to CMH, and a grant in support of research from Petronas Energy Canada (formerly Progress Energy Canada Ltd.). We acknowledge Petronas Energy Canada Ltd., especially Gerry Nyberg, Matt Adams and Wayne Hovdebo for providing access to the large database of XRF analyses c-65-F/94-B-8 and giving us permission to share these findings with the broader geologic community. We also gratefully acknowledge Dr. Mingsong Li for providing his *Acycle* software.

Appendix A. Supplementary data

Supplementary data to this article can be found online at https://doi.org/10.1016/j.palaeo.2026.113915.

Data availability

The authors confirm that all data necessary for supporting the scientific findings of this paper have been provided.

References

Algeo, T., Henderson, C.M., Ellwood, B., Rowe, H., Elswick, E., Bates, S., Lyons, T., Hower, J.C., Smith, C., Maynard, B., Hays, L.E., 2012. Evidence for a diachronous late Permian marine crisis from the Canadian Arctic region. GSA Bull. 124 (9–10), 1424–1448.

Arefifard, S., Algeo, T.J., Zhang, F., Kolar-Jurkovsek, T., Parvizi, T., 2025. A refined biochemostratigraphic framework for the Induan. Palaeogeogr. Palaeoclimatol. Palaeoecol. 668 (June 15), 112902.

Baniak, G.M., Moslow, T.F., Michailides, S., Adams, M.G., 2023. Sequence stratigraphic architecture of the lower Triassic Montney Formation, northeastern British Columbia, Canada. AAPG Bull. 107 (2), 283–310.

Baud, A., Richoz, S., Beauchamp, B., Cordey, F., Grasby, S., Henderson, C.M., Krystyn, L., Nicora, A., 2012. The Buday'ah Formation, Sultanate of Oman: a Middle Permian to early Triassic oceanic record of the Neotethys and the late Indian microsphere bloom. J. Asian Earth Sci. 43, 130–144.

Baud, A., Richoz, S., Brandner, R., Krystyn, L., Heindel, K., Mohtat, T., Mohtat-Aghai, P., Horacek, M., 2021. Sponge takeover from End-Permian Mass Extinction to early Induan Time: records in Central Iran Microbial Buildups. Front. Earth Sci. 9, 586210.

Beatty, T.W., Zonneveld, J.P., Henderson, C.M., 2008. Anomalously diverse early Triassic ichnofossil assemblages in northwest Pangea: a case for a shallow-marine habitable zone. Geology 36 (10), 771–774.

Berger, A., 1988. Milankovitch theory and climate. Rev. Geophys. 26 (4), 624–657.

Boulila, S., Galbrun, B., Miller, K.G., Pekar, S.F., Browning, J.V., Laskar, J., Wright, J.D., 2011. On the origin of Cenozoic and Mesozoic "third-order" eustatic sequences. Earth Sci. Rev. 109 (3–4), 94–112.

Brar, R.S., 2021. Sequence Biostratigraphy and Chronostratigraphy of the Lower Triassic Montney Formation, Northeast British Columbia and West-Central Alberta. Unpublished MSc thesis. University of Calgary, p. 117. pp.

Burgess, S.D., Bowring, S., Shen, S.Z., 2014. High-precision timeline for Earth's most severe extinction. Proc. Natl. Acad. Sci. 111 (9), 3316–3321.

Chen, J., Beatty, T., Henderson, C.M., Rowe, H., 2009. Permian-Triassic boundary at the Dawen Section, Great Bank of Guizhou, Guizhou Province. J. Asian Earth Sci. 36, 442–458.

Cohen, K.M., Finney, S.C., Gibbard, P.L., Fan, J.X., 2013. The ICS international chronostratigraphic chart. Episodes 36 (3), 199–204.

Condon, D.J., Schoene, B., McLean, N.M., Bowring, S.A., Parrish, R.R., 2015. Metrology and traceability of U–Pb isotope dilution geochronology (EARTHTIME Tracer Calibration Part I). Geochim. Cosmochim. Acta 164, 464–480.

Dai, X., Davies, J.H.F.L., Yuan, Z., Brayard, A., Ovtcharova, M., Xu, G., Liu, X., Smith, C. P.A., Schweitzer, C.E., Li, M., Perrot, M.G., Jiang, S., Miao, L., Cao, Y., Yan, J., Bai, R., Wang, F., Guo, W., Song, H.Y., Tian, L., Dal Corso, J., Liu, Y., Chu, D., Song, H.J., 2023. A Mesozoic fossil lagerstatte from 250.8 million years ago shows a modern-type marine ecosystem. Science 379, 567–572.

Dal Corso, J., Ruffell, A., Preto, N., 2019. Carnian (late Triassic) C-isotope excursions, environmental changes, and biotic turnover: a global perturbation of the Earth's surface system. J. Geol. Soc. Lond. 176 (1), 129–131.

Davies, G.R., Moslow, T.F., Sherwin, M.D., 1997. The lower Triassic Montney formation, west-Central Alberta. Bull. Can. Petrol. Geol. 45 (4), 474–505.

Davies, G.R., Watson, N., Moslow, T.F., MacEachern, J.A., 2018. Regional subdivisions, sequences, correlations and facies relationships of the lower Triassic Montney Formation, west-Central Alberta to northeastern British Columbia, Canada—with emphasis on role of paleostructure. Bull. Can. Petrol. Geol. 66 (1), 23–92.

Du, Y., Song, H.J., Algeo, T.J., Song, H., Tian, L., Chu, D., Shi, W., Li, C., Tong, J., 2022. A massive magmatic degassing event drove the late Smithian thermal Maximum and Smithian-Spathian boundary mass extinction. Glob. Planet. Chang. 215, 103878.

Fang, Q., Wu, H., Hinnov, L.A., Jing, X., Wang, X., Jiang, Q., 2015. Geologic evidence for chaotic behavior of the planets and its constraints on the third-order eustatic sequences at the end of the late Paleozoic Ice Age. Palaeogeogr. Palaeoclimatol. Palaeoecol. 440, 848–859.

Fu, W., Jiang, D.Y., Montañez, I.P., Meyers, S.R., Motani, R., Tintori, A., 2016. Eccentricity and obliquity paced carbon cycling in the early Triassic and implications for post-extinction ecosystem recovery. Sci. Rep. 6 (1), 1–7.

Furlong, C.M., Gingras, M.K., Moslow, T.F., Zonneveld, J.P., 2018. The Sunset Prairie Formation: designation of a new Middle Triassic formation between the lower Triassic Montney Formation and Middle Triassic Doig Formation in the Western Canada Sedimentary Basin, Northeast British Columbia. Bull. Can. Petrol. Geol. 66 (1), 193–214.

Galfetti, T., Bucher, H., Ovtcharova, M., Schaltegger, U., Brayard, A., Brühwiler, T., Goudemand, N., Weissert, H., Hochuli, P.A., Cordey, F., Guodun, K., 2007. Timing of the Early Triassic carbon cycle perturbations inferred from new U–Pb ages and ammonoid biochronozones. Earth Planet. Sci. Lett. 258 (3–4), 593–604.

Golding, M.L., 2021. Abundant conodont faunas from the Olenekian (early Triassic) of subsurface British Columbia, Canada and diversification of the Neogondolellinae around the Smithian-Spathian boundary. Glob. Planet. Chang. 205, 103613. https://doi.org/10.1016/j.gloplacha.2021.103613.

Golding, M.L., Orchard, M.J., 2016. New species of the conodont *Neogondolella* from the Anisian (Middle Triassic) of northeastern British Columbia, Canada, and their importance for regional correlation. J. Paleontol. 90 (6), 1197–1211.

Golding, M.L., Orchard, M.J., 2018. *Magnigondolella, a new conodont genus from the Triassic of North America*. J. Paleontol. 92 (2), 207–220.

Golding, M.L., Orchard, M.J., Zonneveld, J.P., Henderson, C.M., Dunn, L., 2014. An exceptional record of the sedimentology and biostratigraphy of the Montney and Doig formations in British Columbia. Bull. Can. Petrol. Geol. 62 (3), 157–176.

Grasby, S.E., Bond, D.P.G., Wignall, P.B., Yin, R., Strachan, L.J., Takahashi, S., 2021. Transient Permian-Triassic euxinia in the southern Panthalassa deep ocean. Geology 49, 889–893.

Guo, G., Tong, J., Zhang, S., Zhang, J., Bai, L., 2008. Cyclostratigraphy of the Induan (early Triassic) in West Pingdingshan Section, Chaohu, Anhui Province. Sci. China Ser. D Earth Sci. 51 (1), 22–29.

Hays, L.E., Beatty, T., Henderson, C.M., Love, G.D., Summons, R.E., 2009. Corrigendum to "evidence for photic zone euxinia through the end-Permian mass extinction in the Panthalassic Ocean (Peace River Basin, Western Canada)". Palaeoworld 18 (1), 74–75.

Henderson, C.M., Baud, A., 1997. The Permian-Triassic Boundary in the Canadian Arctic and a comparison with Meishan China. In: Proceedings of the 30th IGC, Stratigraphy volume, V. 11. VSP Scientific Publishers, pp. 143–152.
Henderson, C.M., Golding, M.L., Orchard, M.J., 2018. Conodont sequence biostratigraphy of the lower Triassic Montney Formation. Bull. Can. Petrol. Geol. 66 (1), 7–22.
Hinnov, L.A., 2000. New perspectives on orbitally forced stratigraphy. Annu. Rev. Earth Planet. Sci. 28 (1), 419–475.
Hinnov, L.A., 2013. Cyclostratigraphy and its revolutionizing applications in the earth and planetary sciences. GSA Bull. 125 (11–12), 1703–1734.
Hinnov, L.A., Hilgen, F.J., 2012. Cyclostratigraphy and astrochronology. Geol. Time Scale 2012, 63.
Hounslow, M.W., Muttoni, G., 2010. The geomagnetic polarity timescale for the Triassic: linkage to stage boundary definitions. Geol. Soc. Lond. Spec. Publ. 334 (1), 61–102.
Huybers, P., Curry, W., 2006. Links between annual, Milankovitch and continuum temperature variability. Nature 441 (7091), 329–332.
Kozur, H.W., Weems, R.E., 2011. Detailed correlation and age of continental late Changhsingian and earliest Triassic beds: implications for the role of the Siberian Trap in the Permian–Triassic biotic crisis. Palaeogeogr. Palaeoclimatol. Palaeoecol. 308 (1–2), 22–40.
Kuhnt, W., Nederbragt, A., Leine, L., 1997. Cyclicity of Cenomanian-Turonian organic-carbon-rich sediments in the Tarfaya Atlantic coastal basin (Morocco). Cretac. Res. 18 (4), 587–601.
Laskar, J., Robutel, P., Joutel, F., Gastineau, M., Correia, A.C.M., Levrard, B., 2004. A long-term numerical solution for the insolation quantities of the Earth. Astron. Astrophys. 428 (1), 261–285.
Laskar, J., Fienga, A., Gastineau, M., Manche, H., 2011. La2010: a new orbital solution for the long-term motion of the Earth. Astron. Astrophys. 532, A89.
Leu, M., Bucher, H., Baud, A., Vennemann, T., Luz, Z., Hautmann, M., Goudemand, N., 2023. An expanded Smithian-Spathian (lower Triassic) boundary from a reefal build-up record in Oman: implications for conodont taxonomy, high-resolution biochronology and the carbon isotope record. Papers Palaeontol. https://doi.org/10.1002/spp2.1481.
Leu, M., Paul, A.N., Bucher, H., Widmann, P., Luz, Z., Vennemann, T., Schaltegger, U., 2025. The early Triassic time scale: new constraints from the Nanpanjiang Basin in South China and a review of geochronological, biostratigraphical and carbon isotope data. Earth Sci. Rev. 267, 105157.
Li, M., Ogg, J., Zhang, Y., Huang, C., Hinnov, L., Chen, Z.Q., Zou, Z., 2016a. Astronomical tuning of the end-Permian extinction and the early Triassic Epoch of South China and Germany. Earth Planet. Sci. Lett. 441, 10–25.
Li, M., Huang, C., Hinnov, L., Ogg, J., Chen, Z.Q., Zhang, Y., 2016b. Obliquity-forced climate during the early Triassic hothouse in China. Geology 44 (8), 623–626.
Li, M., Hinnov, L.A., Huang, C., Ogg, J.G., 2018. Sedimentary noise and sea levels linked to land–ocean water exchange and obliquity forcing. Nat. Commun. 9 (1), 1–12.
Li, M., Song, H., Woods, A.D., Dai, X., Wignall, P.B., 2019a. Facies and evolution of the carbonate factory during the Permian–Triassic crisis in South Tibet, China. Sedimentology 66 (7), 3008–3028.
Li, M., Hinnov, L., Kump, L., 2019b. Acycle: time-series analysis software for paleoclimate research and education. Comput. Geosci. 127, 12–22.
Lourens, L.J., Hilgen, F.J., 1997. Long-periodic variations in the Earth's obliquity and their relation to third-order eustatic cycles and late Neogene glaciations. Quat. Int. 40, 43–52.
Lucas, S.G., 2010. The Triassic timescale: an introduction. Geol. Soc. Lond. Spec. Publ. 334 (1), 1–16.
Meyers, S.R., Sageman, B.B., Arthur, M.A., 2012. Obliquity forcing of organic matter accumulation during Oceanic Anoxic Event 2. Paleoceanography 27 (3).
Moslow, T.F., Haverslew, B., Henderson, C.M., 2018. Sedimentary facies, petrology, reservoir characteristics, conodont biostratigraphy and sequence stratigraphic framework of a continuous (395m) full diameter core of the lower Triassic Montney Fm, northeastern British Columbia. Bull. Can. Petrol. Geol. 66 (1), 259–287.
Neuman, A.G., 2015. Fishes from the lower Triassic portion of the Sulphur Mountain Formation in Alberta, Canada: geological context and taxonomic composition. Can. J. Earth Sci. 52, 557–568.
Ogg, J.G., Chen, Z.Q., Orchard, M.J., Jiang, H.S., 2020. The Triassic period. In: Geologic Time Scale 2020. Elsevier, pp. 903–953.
Orchard, M.J., 2008. Lower Triassic conodonts from the Canadian Arctic, their intercalibration with ammonoid-based stages and a comparison with other north American Olenekian faunas. Polar Res. 27, 393–412.
Orchard, M.J., 2022. North American Spathian (Upper Olenekian, lower Triassic) *Neogondolellin* conodonts. Pap. Palaeontol. 8 (1). https://doi.org/10.1002/spp2.1409.
Orchard, M.J., Zonneveld, J.-P., 2009. The lower Triassic Sulphur Mountain Formation in the Wapiti Lake area: lithostratigraphy, conodont biostratigraphy, and a new biozonation for the lower Olenekian (Smithian). Can. J. Earth Sci. 46, 757–790.
Ovtcharova, M., Bucher, H., Schaltegger, U., Galfetti, T., Brayard, A., Guex, J., 2006. New Early to Middle Triassic U–Pb ages from South China: calibration with ammonoid biochronozones and implications for the timing of the Triassic biotic recovery. Earth Planet. Sci. Lett. 243 (3–4), 463–475.
Ovtcharova, M., Goudemand, N., Hammer, Ø., Guodun, K., Cordey, F., Galfetti, T., Schaltegger, U., Bucher, H., 2015. Developing a strategy for accurate definition of a geological boundary through radio-isotopic and biochronological dating: the Early–Middle Triassic boundary (South China). Earth Sci. Rev. 146, 65–76.
Preto, N., Willems, H., Guaiumi, C., Westphal, H., 2013. Onset of significant pelagic carbonate accumulation after the Carnian Pluvial Event (CPE) in the western Tethys. Facies 59 (4), 891–914.
Raymo, M.E., Nisancioglu, K.H., 2003. The 41 kyr world: Milankovitch's other unsolved mystery. Paleoceanography 18 (1).
Schoepfer, S.D., Henderson, C.M., 2022. Paleogeographic implications of open-marine anoxia in the Permian-Triassic Slide Mountain Ocean. In: Henderson, C.M., Ritter, S., Snyder, W.S. (Eds.), Late Paleozoic and Early Mesozoic Tectonostratigraphy and Biostratigraphy of Western Pangea. SEPM (Society for Sedimentary Geology), Broken Arrow, Oklahoma, pp. 205–225. https://doi.org/10.2110/sepmsp.113.12. Special Publication 113.
Schoepfer, S.D., Henderson, C.M., Garrison, G.H., Ward, P.D., 2012. Cessation of a productive coastal upwelling system in the Panthalassic Ocean at the Permian–Triassic boundary. Palaeogeogr. Palaeoclimatol. Palaeoecol. 313, 181–188.
Schoepfer, S.D., Henderson, C.M., Garrison, G.H., Foriel, J., Ward, P.D., Selby, D., Hower, J.C., Algeo, T.J., Shen, Y., 2013. Termination of a continent-margin upwelling system at the Permian–Triassic boundary (Opal Creek, Alberta, Canada). Glob. Planet. Chang. 105, 21–35.
Schoepfer, S.D., Henderson, C.M., Moslow, T.F., Shen, Chen, 2024. Extremely high resolution XRF core scanning reveals the early Triassic depositional history of the Montney Formation in northeastern British Columbia, Canada. Palaeogeogr. Palaeoclimatol. Palaeoecol. 637, 112019.
Shen, S.Z., Cao, C.Q., Zhang, Y.C., Li, W.Z., Shi, G.R., Wang, Y., Wu, Y.S., Ueno, K., Henderson, C.M., Wang, X.D., Zhang, H., Wang, X.J., Chen, J., 2010. End-Permian mass extinction and palaeoenvironmental changes in Neotethys: evidence from an oceanic carbonate section in southwestern Tibet. Glob. Planet. Chang. 73 (2010), 3–14.
Shen, S.Z., Ramezani, J., Chen, J., Cao, C.Q., Erwin, D.H., Zhang, H., Xiang, L., Schoepfer, S.D., Henderson, C.M., Zheng, Q.F., Bowring, S.A., 2019. A sudden end-Permian mass extinction in South China. GSA Bull. 131 (1–2), 205–223.
Song, H.J., Wignall, P.B., Chen, Z.Q., Tong, J., Bond, D.P., Lai, X., Zhao, X., Jiang, H., Yan, C., Niu, Z., 2011. Recovery tempo and pattern of marine ecosystems after the end-Permian mass extinction. Geology 39, 739–742.
Song, H.J., Wignall, P.B., Tong, J., Bond, D.P.G., Song, H., Lai, X.L., Zhang, K., Wang, H. M., Chen, Y.L., 2012. Geochemical evidence from bio-apatite for multiple oceanic events during Permian-Triassic transition and the link with end-Permian extinction and recovery. Earth Planet. Sci. Lett. 353, 12–21.
Song, H.J., Wignall, P.B., Chu, D.L., Tong, J., Sun, Y.D., Song, H., He, W.H., Tian, L., 2014. Anoxia/high temperature double whammy during the Permian-Triassic marine crisis and its aftermath. Sci. Rep. 4, 4132. https://doi.org/10.1038/srep04132.
Song, H.J., Wignall, P.B., Dunhill, A.M., 2018. Decoupled taxonomic and ecological recoveries from the Permo-Triassic extinction. Sci. Adv. 4 (10), eaat5091.
Sun, Y., Joachimski, M.M., Wignall, P.B., Yan, C., Chen, Y., Jiang, H., Wang, L., Lai, X., 2012. Lethally hot temperatures during the early Triassic greenhouse. Science 338 (6105), 366–370.
Szurlies, M., 2007. Latest Permian to Middle Triassic cyclo-magnetostratigraphy from the central European Basin, Germany: implications for the geomagnetic polarity timescale. Earth Planet. Sci. Lett. 261 (3–4), 602–619.
Tozer, E.T., 1967. A Standard for Triassic Time, 156. Geological Survey of Canada. Bulletin. 103 pp.
Tozer, E.T., 1994. Canadian Triassic Ammonoid Faunas, 467. Geological Survey of Canada. Bulletin. 663 pp.
Widmann, P., Bucher, H., Leu, M., Vennemann, T., Bagherpour, B., Schneebeli-Hermann, E., Goudemand, N., Schaltegger, U., 2020. Dynamics of the largest carbon isotope excursion during the early Triassic biotic recovery. Front. Earth Sci. 8, 196.
Wu, H., Zhang, S., Feng, Q., Jiang, G., Li, H., Yang, T., 2012. Milankovitch and sub-Milankovitch cycles of the early Triassic Daye Formation, South China and their geochronological and paleoclimatic implications. Gondwana Res. 22 (2), 748–759.
Yang, W., Lehrmann, D.J., 2003. Milankovitch climatic signals in lower Triassic (Olenekian) peritidal carbonate successions, Nanpanjiang Basin, South China. Palaeogeogr. Palaeoclimatol. Palaeoecol. 201 (3–4), 283–306.
Zhang, Guijie, Zhang, Xiaolin, Hu, Dongping, Li, Dandan, Algeo, Thomas J., Farquhar, James, Henderson, Charles M., Qin, Liping, Shen, M., Shen, D., Schoepfer, Shane D., Chen, Kefan, Shen, Yanan, 2017. Redox chemistry changes in the Panthalassic Ocean linked to the end-Permian mass extinction and delayed early Triassic biotic recovery. Proc. Natl. Acad. Sci. 114 (8), 1806–1810.
Zhang, L., Orchard, M.J., Brayard, A., Algeo, T.J., Zhao, L., Chen, Z.Q., Lyu, Z., 2019. The Smithian/Spathian boundary (late early Triassic): a review of ammonoid, conodont, and carbon-isotopic criteria. Earth Sci. Rev. 195, 7–36.
Zhang, H.T., Chen, Y., Ogg, J.G., Sun, Z., Wignall, P.B., Wang, M., Zhang, H.X., Zhang, X., Zhang, Y., Huang, K., Lu, H.L., Huang, B., Li, M., 2025. Astronomically calibrated integrated stratigraphy of the Induan Stage (early Triassic) and significance for the Permian-Triassic mass extinction and aftermath. Earth Planet. Sci. Lett. 669, 119563.
Zhao, H., Dahl, T.W., Chen, Z.Q., Algeo, T.J., Zhang, L., Liu, Y., Hu, Z., Hu, Z., 2020. Anomalous marine calcium cycle linked to carbonate factory change after the Smithian thermal Maximum (early Triassic). Earth Sci. Rev. 211, 103418.
Zhu, H., Zhang, G., Li, M.H., Cui, Y., Li, D.D., Sun, L.L., Schoepfer, S.D., Henderson, C.M., Shen, Y., 2025. δ13Corg record from the latest Permian to Middle Triassic in the middle paleo-latitude, Western Canada Sedimentary Basin: global correlation and environmental implications. Palaeogeogr. Palaeoclimatol. Palaeoecol. 662 (15 March), 112741.

Zonneveld, J.P., Moslow, T.F., 2018. Palaeogeographic setting, lithostratigraphy, and sedimentary framework of the lower Triassic Montney Formation of western Alberta and northeastern British Columbia. Bull. Can. Petrol. Geol. 66 (1), 93–127.
Zonneveld, J.-P., Gingras, M., Beatty, T., 2010a. Diverse ichnofossil assemblages following the P-T mass extinction, lower Triassic, Alberta and British Columbia, Canada: evidence for shallow marine refugia on the northwestern coast of Pangaea. Palaios 25, 368–392.
Zonneveld, J.P., MacNaughton, R.B., Utting, J., Beatty, T.W., Pemberton, S.G., Henderson, C.M., 2010b. Sedimentology and ichnology of the lower Triassic Montney Formation in the Pedigree-Ring/Border-Kahntah River area, northwestern Alberta and northeastern British Columbia. Bull. Can. Petrol. Geol. 58 (2), 115–140.